AMERICAN UNIVERSITY OF BEIRUT

Theoretical Analysis of the Trade-off between Power Efficiency and Linearity for Power Amplifiers in Carrier Aggregated Systems

by
Mariam Hassan Issa

A thesis
submitted in partial fulfillment of the requirements
for the degree of Master of Engineering
to the Department of Electrical and Computer Engineering
of the Maroun Semaan Faculty of Engineering and Architecture
at the American University of Beirut

Beirut, Lebanon
January 2019

AMERICAN UNIVERSITY OF BEIRUT

Theoretical Analysis of the Trade-off between Power Efficiency and Linearity for Power Amplifiers in Carrier Aggregated Systems

by

Mariam Hassan Issa

Approved by:

Dr. Hassan Artail, Professor Electrical and Computer Engineering	Advisor
Dr. Ibrahim Abou Faycal, Professor Electrical and Computer Engineering	Member of Committee
Dr. Karim Kabalan, Professor Electrical and Computer Engineering	Member of Committee
Dr. Youssef Nasser, Professor Electrical and Computer Engineering	Member of Committee for Dr. Nasser

Date of thesis defense: January 28, 2019

AMERICAN UNIVERSITY OF BEIRUT

THESIS, DISSERTATION, PROJECT RELEASE FORM

Student Name: Issa (Last) Mariam (First) Hassan (Middle)

☑ Master's Thesis ○ Master's Project ○ Doctoral Dissertation

☐ I authorize the American University of Beirut to: (a) reproduce hard or electronic copies of my thesis, dissertation, or project; (b) include such copies in the archives and digital repositories of the University; and (c) make freely available such copies to third parties for research or educational purposes.

☑ I authorize the American University of Beirut, to: (a) reproduce hard or electronic copies of it; (b) include such copies in the archives and digital repositories of the University; and (c) make freely available such copies to third parties for research or educational purposes after:

One ___ year from the date of submission of my thesis, dissertation or project.

Two ___ years from the date of submission of my thesis , dissertation or project.

Three ___ years from the date of submission of my thesis , dissertation or project.

Mariam Issa (Signature) February/6/2019 (Date)

This form is signed when submitting the thesis, dissertation, or project to the University Libraries

Acknowledgements

I would like to take the opportunity to express my gratitude to Allah for helping me throughout the hardest times, and always gifting me the power and guidance for whats best for me.

Then comes the gratitude for my dear family, my mom Kalthoum, my dad Hassan, my brother Mohammad and my sister Fatima, for always being there next to me and supporting me on all aspects of life. Without them I wouldn't have done anything! They indeed have seen me at my worse and yet never stopped supporting and loving me with all what they have.

Then I would love to express my great happiness for having the opportunity to work with my supervisor professor Hassan Artail. I owe him every success I made and will make in the future. I am grateful to his continuous support, patience, understanding, and motivation on the technical and non-technical sides. He is not only a supervisor, he is a father! I am really blessed to be his research student, and no words are enough to express my sincere gratitude to him.

Also, I thank the members of my respected committee especially professor Ibrahim Abou-Faycal and professor Youssef Nasser for the extremely valuable discussions and meeting that made this work a success.

Finally, the final thanks goes to my dear sister Mona, the 12 years best friend whom always cheered me up whenever I was down, and to my AUB sisters Reem, Aya, Sophie, Rosette, Rasha, Salam, Carine, Farah, Alaa and Kawthar for adding to the AUB experience the amazing memories and the precious moments that I will hold with me through my life.

An Abstract of the Thesis of

Mariam Hassan Issa for Master of Engineering
Major: Electrical and Computer Engineering

Title: Theoretical Analysis of the Trade-off between Power Efficiency and Linearity for Power Amplifiers in Carrier Aggregated Systems

The bandwidth and data rate gains achieved by carrier aggregation led to its evolution through LTE releases R10 (LTE-Advanced) to R15 (5G NR). However, the aggregation of multiple OFDM and SC-FDMA signals suffer from high Peak-to-Average-Power-Ratio (PAPR), which in turn affects the High Power Amplifier (HPA) by inducing non-linearities and causing deterioration in the power efficiency, in band and out of band distortions. However, there exists a fundamental trade-off between power efficiency and linearity in the High Power Amplifier. This complicates the design of a high performing system on both aspects. This thesis serves to present a Carrier Aggregated OFDM system that combines PAPR reduction with Digital Predistortion to achieve a good trade-off between efficiency and linearity.

Towards meeting this goal, we thus follow a three step process where we first analyze and reduce the PAPR of the CA-OFDM system by deriving the probability distribution of PAPR in CA-OFDM systems and proposing a new PAPR reduction method. Then we study existing linearization techniques and apply the well-known technique of Digital Predistortion (DPD). Finally, we combine the proposed PAPR reduction method with DPD to study the overall system performance.

Our obtained results indicate that combining PAPR reduction and Digital Predistortion enhances the performance of the system in terms of lowering the Adjacent Channel Power Ratio and reducing the needed Input backoff thus increasing the power efficiency.

Contents

List of Figures

List of Tables

Chapter 1

Introduction

Most of the advancements in communications share the common goals of increasing the data rates and bandwidths of the users, with reducing power consumption as much as possible, in addition to guaranteeing reliable and distortion-less transmissions. However, these goals come on top of complications in designs of the transceivers and induce stringent trade-offs between cost and performance. These design aspects are tackled in Baseband and in the RF front end of both transmitters and receivers.

However, the exponential growth of mobile data can be better managed through the efficient spectrum utilization by using Carrier Aggregation (CA). This feature first appeared in LTE release 10, where multiple SC-FDMA signals can be aggregated in the uplink to allow a peak data rate of 500 Mbps, and multiple OFDM signals can be aggregated in the downlink to yield a peak data rate up to 1 Gbps. The large gains offered by CA allowed its deployment to evolve with later releases of LTE, up to release 15. Release 11 proposed aggregation of carriers across cells as in the case of Heterogeneous Networks (HetNets). Then aggregation of TDD carriers with FDD carriers was proposed in Release 12. Release 13 came with Enhanced Carrier Aggregation (eCA) where the number of aggregated carriers increased from 5 up to 32. Aggregation of carriers across licensed and unlicensed bands was proposed beyond release 12.

Unfortunately, the aggregation of SCFDMA and OFDM signals comes at the cost of increasing the Peak-To-Average-Power-Ratio (PAPR) of the resultant signal due to the high fluctuation of the aggregated signal envelope. A large PAPR causes non-linearities in the High Power Amplifier (HPA) used in the RF chain. Figure 4.1 shows the transmitter architecture of the carrier aggregated system that we adopt in this thesis.

Intuitively, a possible solution to the PAPR problem would be reducing the signal peak power by backing off the input power; however this is not an efficient solution as it decreases the efficiency of the system. Thus the PAPR problem should be tackled in a way that does not decrease the power efficiency. This complicates the design of an efficient power amplifier with high linearity.

Therefore, there is a need to carefully consider these two aspects in the High Power Amplifier (HPA) design. In order to alleviate the PAPR and the linearity problem, two blocks should be added prior to the PA; these are PAPR reduction and linearization blocks as shown in the block diagram of the system in Figure 1.1. Nevertheless, it is well known that there exists a fundamental tradeoff between achieving power efficiency and high linearity. These two problems are in most of the cases treated independently in literature.

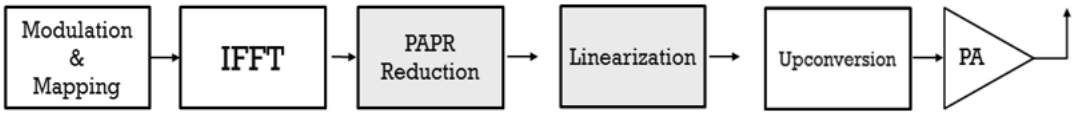

Figure 1.1: Transmitter Flow Diagram

This thesis and its future work serve to study the mutual relation between PAPR reduction and Linearization. The literature is full of works that study PAPR reduction and linearization each one independently, however since there had been some works that highlighted the performance gain attained from combining PARR reduction with linearization, many works started to appear within this context.

1.1 Thesis Objectives and Outline

1.1.1 Thesis Objectives

In this thesis, we aim to study this relation for a Carrier Aggregated OFDM system, where we adapt an LTE-Advanced transmitter. In order to meet this goal, we followed a three step process:

1. We tackle the power efficiency problem through PAPR reduction.
2. We tackle the linearity problem through Digital Predistortion (DPD).
3. We combine both PAPR reduction and DPD, and then we study the final performance.

1.1.2 Thesis Outline

The aforementioned three step process can be outlined as follows:

A) PAPR Analysis and Reduction:

1. Analyzing the probability distribution of PAPR in CA-OFDM systems where we proposed an expression that approximates this distribution using the Level Crossing Rate (LCR) analysis.

2. Demonstrating the application of the derived expression to model the known PAPR reduction method Selective Mapping Technique (SLM).

3. Proposing a new lower complexity, high performance PAPR reduction technique for CA-OFDM systems referred to as Peak Valley Alignment, while incorporating some of the expressions obtained in the previous step.

4. Studying the performance of the proposed PVA through PAPR reduction capability, increase in coverage area gain due to PAPR reduction and through deriving the computational complexity of PVA and comparing it to the other existing techniques in literature.

B) Linearization through Digital Predistortion:

1. Conducting a literature review about exiting Linearization techniques: Digital Predistortion (DPD), their challenges and their solutions.

2. Implementing and apply DPD to our CA-OFDM signals.

3. Studying the performance of the system with and without DPD in terms of spectral regrowth suppression and Adjacent Channel Power Ratio (ACPR) reduction.

C) Combining PAPR Reduction and Digital Predistortion:

1. Studying the performance of the system with PAPR reduction and DPD.

2. Finding the trade-off offered by the proposed PVA on power efficiency and Linearity.

The chapters are divided as follows: in chapter 2, we define the system model and define the PAPR problem formulation. In chapter 3, PAPR is analyzed through its probability distribution. Then in chapter 4, we propose the aforementioned Peak Valley Alignment technique, where its performance is studied in details. After that chapter 5 serves as a study on digital predistortion and its application to our system. Then chapter 6 studies the combination of PAPR reduction and DPD. Finally the thesis conclusion and future directions are provided in chapter 7.

Chapter 2

System Model and Problems Formulation

2.1 Chapter Introduction

In this chapter we provide the system model and formulate the PAPR and Linearization problems. We base our analysis on an LTE-Advanced (LTE-A) system.

In the LTE-A standard, several release 8 CCs can be aggregated together, where aggregation comes in two forms: contiguous and non-contiguous. In section 2.1 we present the time domain equations for the CA-OFDM signal, define the PAPR problem in section 2.2 and the linearity problem in section 2.3.

2.2 CA-OFDM signal Representation

We let $X_{i,\mu,k}$ denote the set of complex data symbols for the μ^{th} OFDM symbol in the i^{th} CC, where $i = 1, ..., CC_{nb}$ denotes the index of the component carrier (CC) and CC_{nb} denotes the total number of CCs, $\mu = 0, 1, ..., N_{sym}$ signifies the index of the OFDM symbol where N_{sym} stands for the number of OFDM symbols used, and $k = 0, ..., N-1$ is the subcarrier index. Also, we let f_i denote the frequency difference between the center frequency of the i^{th} CC and the first CC. The complex continuous baseband signal for the i^{th} CC defined over the time interval $t \in [0, T_s]$ can be expressed as:

$$s_i(t) = x_i(t) + jy_i(t) = \frac{1}{\sqrt{N}} \sum_{k=0}^{N-1} X_k e^{j2\pi \frac{k}{T_s} t} \tag{2.1}$$

where T_s is the OFDM symbol period. The aggregated signal is then given by

$$s_{Agg}(t) = x_{Agg}(t) + jy_{Agg}(t) = \frac{1}{\sqrt{N}} \sum_{i=1}^{CC_{nb}} s_i(t) e^{j2\pi f_i t} \tag{2.2}$$

and $x_i(t), y_i(t), x_{Agg}(t), y_{Agg}(t)$ denote the real and the imaginary parts of the signals in (2.1) and (2.2) respectively. The n^{th} sample of the discrete baseband CA-OFDM signal is:

$$s_{Agg}(t) = s_{Agg}(\frac{nT_s}{N}) \tag{2.3}$$

and the resulting discrete time signal can be represented as

$$s_{Agg}[n] = x_{Agg}[n] + jy_{Agg}[n] \tag{2.4}$$

The output of the inverse fast Fourier transform (IFFT) is the complex baseband discrete time signal that corresponds to the μ^{th} OFDM symbol of the i^{th} CC in a certain subframe. It is given by:

$$s_i[n] = \frac{1}{\sqrt{N}} \sum_{k=0}^{N-1} X_{i,\mu,k} e^{j2\pi \frac{kn}{N}} e^{j2\pi f_i n} \tag{2.5}$$

where N corresponds to the IFFT size, and $n = 0, 1...N-1$. The aggregated OFDM signal of all the CCs is given by:

$$s_{Agg}[n] = \frac{1}{\sqrt{N}} \sum_{i=1}^{CC_{nb}} \sum_{k=0}^{N-1} X_{i,\mu,k} e^{j2\pi \frac{kn}{N}} e^{j2\pi f_i n} \tag{2.6}$$

We note that the cyclic prefix (CP) will be ignored as it does not affect the PAPR calculations, and no pulse shaping is used. The data symbols are assumed to be statistically independent, identically distributed ($i.i.d$) random variables with zero mean and variance $\sigma_X^2 \hat{=} E[|X_k|^2]$. The signal $s_i(t)$ corresponding to the i^{th} CC follows a Gaussian distribution with zero mean and variance $\sigma_s^2 = \sigma_X^2 =$ by the central limit theorem since it is the sum of $Ni.i.d$ random variables [1]. On the other hand, the aggregated signal is the sum of CC_{nb} independent normally distributed random variables, each with zero mean and variance σ_X^2. Thus leading the continuous processes $x_{Agg}(t)$ and $y_{Agg}(t)$ to become Gaussian distributed with zero mean and variance $\frac{CC_{nb}\sigma_X^2}{2}$. Consequently, $x_{Agg}(t)$ and $y_{Agg}(t)$ are uncorrelated Gaussian random variables. Furthermore, we assume that $x_{Agg}(t)$ and $y_{Agg}(t)$ are independent. Hence, the envelope process $r_{Agg}(t)$ will follow a Rayleigh distribution. As a result, one can infer that the carrier aggregated OFDM signal holds the same statistical properties as those of the non-aggregated OFDM signal [2].

2.3 The PAPR Problem Formulation

The Peak-To-Average-Power-Ratio (PAPR) of the baseband aggregated OFDM signal PAPR can be defined as

$$PAPR = \frac{\max\limits_{0 \le t \le T_s} |s_{Agg}(t)|^2}{P_{avg}} \tag{2.7}$$

where P_{avg} is the average power of the aggregated baseband signal. In order to measure the PAPR performance, the complementary cumulative distribution function (CCDF) is used. It allows to evaluate the statistical characteristics of the PAPR by estimating the probability of PAPR to exceed a certain PAPR level, defined as $PAPR_0$. The CCDF expression of the PAPR then can be written as $CCDF = Pr(PAPR > PAPR_0)$.

2.4 The Linearity Problem Formulation

The term linearity stems from an amplifiers linear relationship of input power to output power. Ideally, this relation should be linear and is characterized by a constant gain. Practical powers amplifiers are not ideal in their transfer characteristics and can generate harmonic signals at multiples of the applied fundamental input signals, both of which are amplified along with the desired tones thus creating intermodulation distortion (IMD). In order to achieve linearity, and avoid carrier inter-modulations with respecting the power mask, additional circuitry is needed. These additions are referred to as linearization blocks, where the most common technique is digital Predistortion (DPD).

A non-careful treatment of HPA leads to undesirable results that appear in the form of distortion to the signals, induction of interference to other bands and decreased power efciency of the system. Ideally, the input and output of the PA are related by a constant referred to as gain. In practice, this relation does not hold, and the relation between the output and input is not linear, thus leading to the aforementioned problems.

Non-linear ampliers cause inter-modulation distortion (IMD) products which are harmonics outside the desired bandwidth. In other words, nonlinear distortion creates undesired signal energy at frequencies outside the bandwidth of the original signal. Filtering cannot easily eliminate IMD products since they are located on the same frequency or near to the desired input signals. Unwanted spectral regrowth yields to interference with adjacent channels. In addition, power ampliers are usually operated in the nonlinear region right before saturation in order to achieve maximum power efciency which leads to distortion and spectral regrowth. In general, distortion is produced by amplitude and phase non-linearity [**24**]. Contrarily, high linearity can provide transmission of information with spectral efciency. Since IMD products are produced by a loss of linearity, various linearization techniques have been developed for the cancellation of distortion. Exhaustive research has been done and is still running in order to mitigate the effect of non-linearities in HPAs.

2.5 Chapter Conclusion

In this chapter we presented the system model by presenting the time domain equations of the CA-OFDM system. Then we have shown that the CA-OFDM signal holds the same statistical properties of the non-aggregated signal, thus the same assumptions hold in both aggregated and non-aggregated cases. After that, we defined the PAPR metric and justified the methodology of its analysis. Finally, we briefly introduced the linearity problem and the need to mitigate it. In the next chapter, we analyze the probability distribution of the PAPR in CA-OFDM systems.

Chapter 3

PAPR Analysis in Carrier Aggregated OFDM Systems

3.1 Chapter Introduction

As stated in chapter 1, power efficiency will treated through PAPR reduction. The objective of this chapter is to provide an analysis of the probability distribution of PAPR in CA-OFDM systems. We therefore present a literature review on the works that analyzed the PAPR in OFDM systems, and demonstrates a proposed expression that approximates the probability distribution of PAPR using Level Crossing Rate analysis for CA-OFDM systems ([2]) .

The PAPR problem has been arising since the early applications of OFDM, and it became a more serious issue with carrier aggregation in both CA-SC-FDMA and CA-OFDM. Many previous works have tackled the problem of PAPR, and proposed several reduction techniques. However, prior to describing such techniques, the properties of PAPR should be well understood for a better theoretical assessment of PAPR reduction, and for an effective system design that involves non-linear devices. Such knowledge helps in quantifying the fundamental trade-off between power efficiency and linearity, which will be the topic of this thesis and its future work.

The PAPR should be tackled probabilistically since the aggregated signal is generated by a random process, i.e., the probability distribution of the PAPR should be characterized. The literature is rich in works that specifically analyze the statistics of PAPR in both OFDM [3] [4] [5] [1] [6] [7] [8] [9], and SC-FDMA [10] [11] [12] [13] [14] [15]. However, no similar work has been done for the case of carrier-aggregated signals, thus the motivation of the work presented in this chapter.

The key aspect of OFDM related analysis is that the OFDM signal can be assumed to be Gaussian distributed, and thus its envelope obeys a Rayleigh distribution, under the assumption that the real and the imaginary parts of the

signals are independant. This is because the composite time domain signal is the sum of i.i.d uncorrelated random variables. However, this cannot be the case for SC-FDMA as proved in [10]. Although the uplink is more power constrained than the downlink, it is still a valid problem to study the PAPR in the downlink, since this increased PAPR can adversely affect the receiving devices energy efciency. Moreover, if its power amplier was not designed to handle the increased PAPR, it could result in performance degradations and out-of-band spectral leakage if the linearity range of the amplier is not sufcient to handle it [16].

Our work in this chapter models the distribution of PAPR in the downlink for Carrier Aggregated Orthogonal Frequency Division Multiplexing (CA-OFDM) signals based on the technique of Rice [17], which is known as the Level Crossing Rate (LCR) method. Despite the simplicity of this technique, it is an almost accurate approximation of the peak statistics as will be explained throughout this chapter.

In summary, the technique allows to count the number of peaks by counting the number of crossings of a certain threshold level. Ochiai in [1] successfully applied this technique to non-aggregated OFDM signals, hence the motivation behind adopting LCR in our work. For completeness and ease of discussion, we provide in the next section a brief summary on the concept of Level Crossing Rate.

3.2 Level Crossing Rate (LCR): An Approximation for Peaks Distribution in a signal

The main motivation behind this approach is that it offers a simple yet accurate approximation for the peak distribution in the signal, without having to deal with the derivation of the peak distribution, which gets quite complicated. Stated shortly, the number of peaks can be approximated by the number of upward crossings of a certain threshold reference level. However, this is true under two assumptions. The first one is that the signal is band-limited, while the second constrains the choice of the threshold reference level. These assumptions will be made clear in what follows. LCR was proposed by Rice in [17] to obtain threshold crossing statistics from the joint distribution $p(x, x)$ for a stochastic process $x(t)$.

As explained in [18], this joint distribution helps in determining whether a combination of $x(t)$ and $x(t)$ will yield a crossing to level l during the interval between t and $t + \delta t$. In simple terms, the LCR gives the number of times the process exceeds a given threshold in a given period of time. As stated in [18], the LCR for a level l can be obtained by solving the integral

$$V^{+}{}_{c}(l) = \int_{0}^{\infty} \dot{x} p(l, \dot{x}) d\dot{x} \tag{3.1}$$

The mean number of peaks above level l is denoted by

$$\bar{N}_p(l) \approx {v^+}_c(l) T_s \tag{3.2}$$

For a band-limited Gaussian random process, the probability that a peak is above level l is given by [18]:

$$P_r(\rho > l) \approx \frac{{v^+}_c(l)}{{v^+}_c(0)} \tag{3.3}$$

The term ${v^+}_c(l)$ represents the rate of zero crossings, i.e. rate of all positive slope zero crossings. This expression is validated in [18], because for a band-limited Gaussian process, each cycle from one positive peak to another contains a single peak.

3.3 Related Works on PAPR Distribution

Researchers in this area followed two main tracks. In the first track, authors derived upper bounds on the PAPR for OFDM [3] [9] and for SC-FDMA [10] [11] . However, such studies cannot always give sufficient statistics since as the number of subcarriers in an OFDM signal increases, the probability of occurrence of the theoretically maximum PAPR becomes negligible.

In the second track, the statistical distribution of the PAPR was tackled, and two main contributions can be identified within this track. The first can be referred to as Gaussian Approximation and was proposed in [4], although it lacked complete accuracy due to the inadequate modeling of oversampling. The expression of the PAPR CDF distribution was given by

$$F_p(P) = (1 - e^{-P})^N \tag{3.4}$$

Later, an extension was proposed in [5] which included an empirical modification to the expression in 3.5 to accommodate oversampling:

$$F_p(P) = (1 - e^{-P})^{\alpha N} \tag{3.5}$$

Where α was found to be 2.8 using computer simulations. Although this expression proved to be accurate, it lacks theoretical justification for the α parameter.

The other main contribution was introduced in [1], where the authors applied the Rice method of the LCR to approximate the distribution of PAPR. This method was shown to be simple and accurate without having to care about oversampling. In addition to the Gaussian assumption for the distribution of the signal, another assumption regarding a reference threshold level $\bar{r}$ was needed so that the number of crossings to this level approaches the number of peaks.

A proper choice of $\bar{r}$ guarantees this requirement. This is because the envelope process of interest is Rayleigh and not Gaussian. Hence, $\bar{r}$ should be chosen such that the distribution of the CF is conditioned on crossing this level $\bar{r}$. As in [1], 3.6 can be approximated for $r > \bar{r}$ by:

$$P_r(\rho > r|\rho > \bar{r}) = \frac{\bar{N}_p(r)}{\bar{N}_p(\bar{r})} \approx \frac{{v^+}_c(l)T_s}{{v^+}_c(l)T_s} = \frac{{v^+}_c(l)}{{v^+}_c(l)} \tag{3.6}$$

It was also assumed there that the peaks are conditionally independent, given that a sample of the envelop process is higher than the reference level ($\bar{r}$. Thus the conditional probability of the CF was given by

$$P_r(C > r|C > \bar{r}) = P_r(\rho < r|\rho < \bar{r})^{N_p} \tag{3.7}$$

Where N_p is the number of peaks in the signal. However, as the number of subcarriers becomes large, the number of peaks observed in one sample approaches its mean value with a probability of 1 by the law of large numbers, so the expression in 3.8 becomes

$$P_r(r|C > \bar{r}) = P_r(\rho < r|\rho < \bar{r})^{\bar{N}_p} \tag{3.8}$$

The authors in [1] derived the expression of ${v^+}_c(r)$ for the Rayleigh process and showed it to be

$${v^+}_c(r) = \sqrt{\frac{\pi}{3}}\frac{N}{T_s} r e^{-r^2} \tag{3.9}$$

and $\bar{N}_p = {v^+}_c(r)T_s$ Thus the expression of the CF CDF of non-aggregated OFDM signal could be written as:

$$F_c(r) \approx F_c(r|C > \overline{r}) = \begin{cases} \left(1 - \dfrac{re^{-r^2}}{\overline{r}e^{-\overline{r}^2})}\right)^{\sqrt{\frac{\pi}{3T_s}\overline{r}e^{-\overline{r}^2}}} & \text{for } r > \overline{r} \end{cases} \tag{3.10}$$

and 0 otherwise. As for the reference level $\bar{r}$, it was found that a value around $\sqrt{\pi}$ gives a good agreement between the simulation results and the proposed expression.

On the other hand, the authors in [6] used the Extreme Value theory approach to model the distribution of PAPR for OFDM signals, where in a later work [19], they gave a full proof for the convergence of the OFDM signal process to a Gaussian random process. They derived the expression of the PAPR distribution which, is given in [6] :

$$P\left\{P_N \leq y\right\} \cong \exp\left\{-e^{-yN\sqrt{\frac{\pi}{3}\log N}}\right\} \tag{3.11}$$

Knowing that the authors in [6] gave a rigorous proof for the convergence of the signal process and the PAPR distribution derivation, our goal in this work is

to determine an expression for the PAPR distribution of the CA-OFDM signal in a simple way with justifiable assumptions. We adopt the LCR approach due to its simplicity and direct relevance for approximating the distribution of the PAPR in OFDM signals, thus we are extending the work of [1] to match our case.

In addition to the aforementioned works, the works in [7][8][9] analyzed non-contiguous OFDM (NC-OFDM), where specific block(s) of subcarriers are intentionally deactivated, thus creating frequency gap(s) in the spectrum of the transmitted signal. As explained in [7], the distribution of PAPR in NC-OFDM signals is different than that of OFDM since it depends on the subcarrier spacing, which introduces dependence among the subcarriers, thus omitting the common assumption that the input symbols are i.i.d used in OFDM systems. However, there is a similarity in spectrum between aggregated OFDM signals and Non-Contiguous OFDM signals. That is, both exhibit constant-level PSD levels separated by gaps.

In our case, we are modeling aggregation of contiguous OFDM signals and further understanding of NC-OFDM is left for the reader.

3.4 Proposed Distribution Modeling of PAPR in CA-OFDM

As demonstrated using the system model, it was shown that statistically, both aggregated and non-aggregated OFDM signals hold the same properties. For this, we extend the technique of LCR in [1] to study the PAPR distribution of aggregated OFDM signals by following the same steps, while accounting for the multiple bands and the separations between them. We derive in this section the expression of the CDF for CA-OFDM signals for two component carriers (CCs) first, and then provide a generic expression for an arbitrary number and size of component carriers and gaps. The envelope $r(t)$ of the carrier-aggregated OFDM signal is given by (9). The processes $x_{Agg}(t), y_{Agg}(t), \dot{x}_{Agg}(t), \dot{y}_{Agg}(t)$ are statistically independent stationary Gaussian random processes with zero mean and variances ${\sigma_x}^2, {\sigma_y}^2, \sigma_{\dot{x}}^2, \sigma_{\dot{y}}^2$ respectively, since the derivative operation is linear. The joint PDF of the samples of $x_{Agg}(t), y_{Agg}(t), \dot{x}_{Agg}(t), \dot{y}_{Agg}(t)$ processes is given by

$$f_{x,y}(X) = \frac{1}{\sqrt{(2\pi)^n |R|}} e^{\left[-\frac{1}{2} X R^{-1} X^t\right]} \tag{3.12}$$

Where $x_{Agg}(t), y_{Agg}(t), \dot{x}_{Agg}(t), \dot{y}_{Agg}(t)$, $n = 4$, and R is the covariance matrix whose determinant is $|R|$ and its value is:

$$R = \begin{bmatrix} \sigma_x^2 & 0 & 0 & 0 \\ 0 & \sigma_x^2 & 0 & 0 \\ 0 & 0 & \sigma_x^2 & 0 \\ 0 & 0 & 0 & \sigma_x^2 \end{bmatrix} \tag{3.13}$$

where

$$\begin{array}{c} E\left[x_{Agg}(t)x_{Agg}(t)\right] \triangleq \sigma_x^2 \\ E\left[\dot{x}_{Agg}(t)\dot{x}_{Agg}(t)\right] \triangleq \sigma_x^2 \end{array} \tag{3.14}$$

$$E\left[x_{Agg}(t)\dot{x}_{Agg}(t)\right] = 0.5\frac{d}{dt}E\left[x_{Agg}(t)^2\right] = 0$$

switching into polar coordinates, where $x_{Agg} = \sqrt{2\pi\sigma_x^2}r\cos\theta$ and $y_{Agg} = \sqrt{2\pi\sigma_x^2}r\sin\theta$, The joint PDF in terms of $r, \theta, \dot{r}$ and $\dot{\theta}$ becomes

$$f_{r,\theta}(r,\dot{r},\theta,\dot{\theta}) = \frac{r^2}{\pi^2 K}e^{\left[-r^2-\frac{1}{K}\left(\dot{r}^2+r^2\dot{\theta}^2\right]\right.} \tag{3.15}$$

where K is defined to be

$$K \triangleq \frac{\sigma_x^2}{\sigma_x^2} \tag{3.16}$$

Solving the integral of 3.17 gives 3.18 which gives the expression of the joint distribution of the envelope process and its derivative.

$$\int_0^{2\pi}\int_{-\infty}^{\infty} f_{r,\theta}(r,\dot{r},\theta,\dot{\theta})d\theta d\dot{\theta} \tag{3.17}$$

$$f_r(r,\dot{r}) = 2re^{-r^2}\frac{1}{\sqrt{\pi K}}e^{-\frac{\dot{r}^2}{K}} \tag{3.18}$$

3.4.1 Expression for Two Component Carriers (CC=2)

Now, we find $\sigma_{\dot{x}}^2$ in terms of ${\sigma_x}^2$ before plugging them both into the expression for K:

$$\begin{array}{c} \sigma_x^2 = \int_{-\infty}^{\infty} S_x(f)df \\ \sigma_{\dot{x}}^2 = \int_{-\infty}^{\infty}(2\pi f)^2 S_x(f)df \end{array} \tag{3.19}$$

In the above expression, $S_x(f)$ denotes the power spectral density (PSD) of $x_{Agg(t)}$. The PSD of the carrier aggregated OFDM signal is analogous to that of the non-aggregated signal, where the PSD of each CC is equally distributed over the band but with the existence of gaps that correspond to the component carrier spacing. These gaps appear in the expression of the variance σ_x^2 . Figure 3.1 shows that the plot of the PSD of the CA-signal for 1.4MHz/CC which appears to be band limited. The letters in Figure 3.1 represent the edges of each CC. We let $A = 0, B = w_1, C = w_1 + g$ and $D = w_1 + g + w_2$. We denote by w_i the bandwidth corresponding to i^{th} Component Carrier (CC). With these definitions, the expression of the PSD can be written as

$$x(f) = \begin{cases} \frac{\sigma_x^2}{w_1^1} f \epsilon w1 \\ \frac{\sigma_x^2}{w2} f \epsilon w2 \\ 0otherwise \end{cases} \tag{3.20}$$

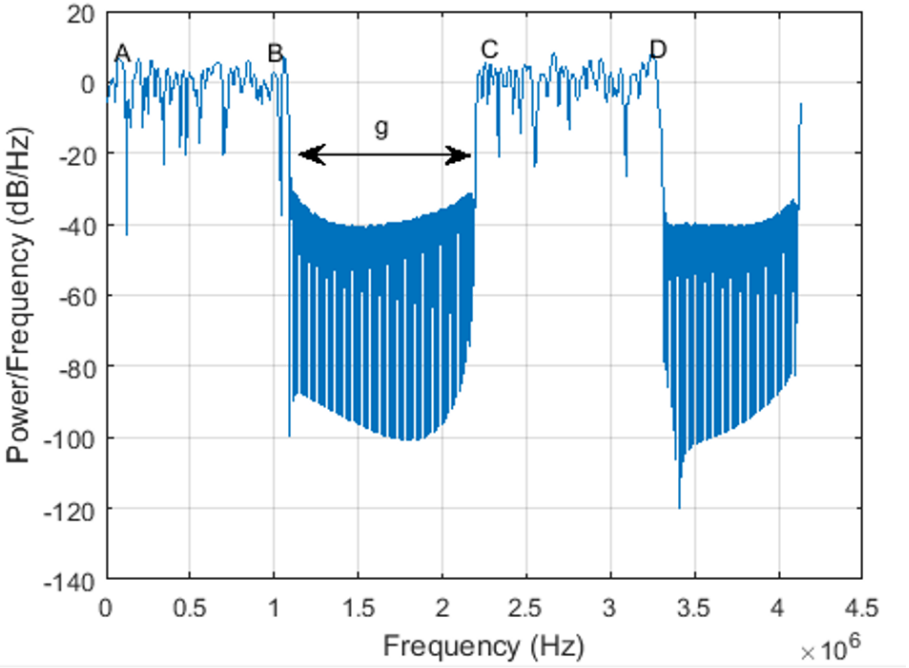

Figure 3.1: PSD of CA-OFDM signal CC=2

The integral in 3.20 for $\sigma_{\dot{x}}^2$ can be then written as

$$\sigma_{x'}^2 = \int_0^{w_1} (2\pi f)^2 \frac{\sigma_x^2}{w_1} df + \int_{w_1+g}^{w_1+g+w2} (2\pi f)^2 \frac{\sigma_x^2}{w_1} df \tag{3.21}$$

Solving the integral and plugging the answer in the expression of K, we get

$$K \triangleq \frac{\sigma_{x'}^2}{\sigma_x^2} = \frac{4\pi^2}{3} w_1^2 + 4\pi^2 K_1 + 4\pi^2 w_2 \sqrt{K_1} + 4\pi^2 w_2^2 \tag{3.22}$$

with $_1 = (w_1 + g)^2$. Recall that the level crossing rate is given by

$$v_c^+(l) = \int_0^\infty \dot{x} p(a, \dot{x}) d\dot{x} = \int_0^\infty \dot{r} f_r(a, \dot{r}) d\dot{r} \tag{3.23}$$

and the mean number of peaks is found by $\bar{N}_{p(\bar{r})} = v_{c,Agg}^+ T_s$. Plugging 3.22 in 3.18 and solving the right hand side integral in 3.23, yields 3.24:

$$v_{c,Agg}^+(l) = \sqrt{\frac{\frac{4\pi^2}{3} w_1^2 + 4\pi^2 K_1 + 4\pi^2 w_2 \sqrt{K_1} + 4\pi^2 w_2^2}{\pi}} l e^{-l^2} \tag{3.24}$$

To continue with the derivation, the conditional CDF of the CF becomes

$$F_c(r|C > \overline{r}) = \Pr(\rho < r | \rho > \overline{r})^{\overline{N_p(r)}} = \left(1 - \frac{r e^{-r^2}}{\overline{r} e^{-\overline{r}^2}}\right)^{\overline{N}_{p(r)}} \tag{3.25}$$

So, for a band-limited CA-OFDM signal, the expression of the distribution of the crest factor (CF) is given by

$$F_c(r) \approx F_c(r|C > \bar{r}) = \left(1 - \frac{re^{-r^2}}{\bar{r}e^{-\bar{r}^2}}\right)^{T_S \sqrt{\frac{\frac{4\pi^2}{3}w_1^2 + 4\pi^2 K_1 + 4\pi^2 w_2 \sqrt{K_1} + 4\pi^2 w_2^2}{\pi}} \bar{r}e^{-\bar{r}^2}} \tag{3.26}$$

when $r > \bar{r}$, and is 0 otherwise. To obtain the distribution of the PAPR, a change of variable $\mu = r^2$ should be applied.

3.4.2 Arbitrary Number of CCs and Gap Size

The need for a larger bandwidth will continue to evolve, and more component carriers will need to be allocated in non-uniform schemes according to the available bandwidth. Thus, we need a generic expression that accounts for any resource allocation scheme. For a generic number of CCs and arbitrary spacing size, we denote by w_j the bandwidth spanned by the j^{th} CC, and by g_j the component carrier spacing between two consecutive CCs. The expression of the power spectral density becomes

$$Sx(f) = \begin{cases} \frac{\sigma_x^2}{w_j} & f \in w_j \\ 0 & 0.w \end{cases} \tag{3.27}$$

while the expression of $\sigma_{\dot{x}}^2$ will be

$$\sigma_{\dot{x}}^2 = \sum_{j=1}^{Ncc} \int_{\sum_{i=0}^{j-1} w_i + g_i}^{w_j + \sum_{i=0}^{j-1} w_i + g_i} (2\pi f)^2 \frac{\sigma_x^2}{w_j} df \tag{3.28}$$

Consequently, K becomes

$$K = \sum_{j=1}^{Ncc} \int_{\sum_{i=0}^{j-1} w_i + g_i}^{w_j + \sum_{i=0}^{j-1} w_i + g_i} (2\pi f)^2 \frac{1}{w_j} df \tag{3.29}$$

The distribution of the CF follows by following the same steps as above after using the derived value of K, and is given by 3.30:

$$\left(1 - \frac{re^{-r^2}}{\bar{r}e^{-\bar{r}^2}}\right)^{T_S \sqrt{\frac{\sum_{j=1}^{Ncc} \int_{\sum_{i=0}^{j-1} w_i + g_i}^{w_j + \sum_{i=0}^{j-1} w_i + g_i} (2\pi f)^2 \frac{1}{w_j} df}{\pi}} \bar{r}e^{-\bar{r}^2}} \tag{3.30}$$

For $r > \bar{r}$ and 0 otherwise.

3.5 Simulation Results

The simulation of contiguous and non-contiguous CA-OFDMA was carried out for minimal (1.4MHz/CC) and maximal (20MHz/CC) bandwidths for CC=2 and CC=5, as stated in Release 8 of LTE for each CC. The component carrier spacing in the contiguous case is the minimal spacing of 300 KHz in order to guarantee backward compatibility with earlier releases and to preserve the orthogonality among the OFDM subcarriers, and it is 3MHz for the non-contiguous case, which is an integer multiple of 300KHz. The modulation used is Rectangular 16-QAM, and the continuous time signal is approximated by using an oversampling factor of 4 as suggested in [20], where a minimum value of 4 is sufficient.

3.5.1 Determining The Reference Level

It shall be noted that $= {v^+}_{c,Agg}(l) > {v^+}_{c,Non-Agg}(l)$, i.e., the aggregated signal has more level crossings per unit time than those of the non-aggregated signal, and the problem of having a single peak within each crossing is still existent. The key factor is the threshold reference level $\bar{r}$.

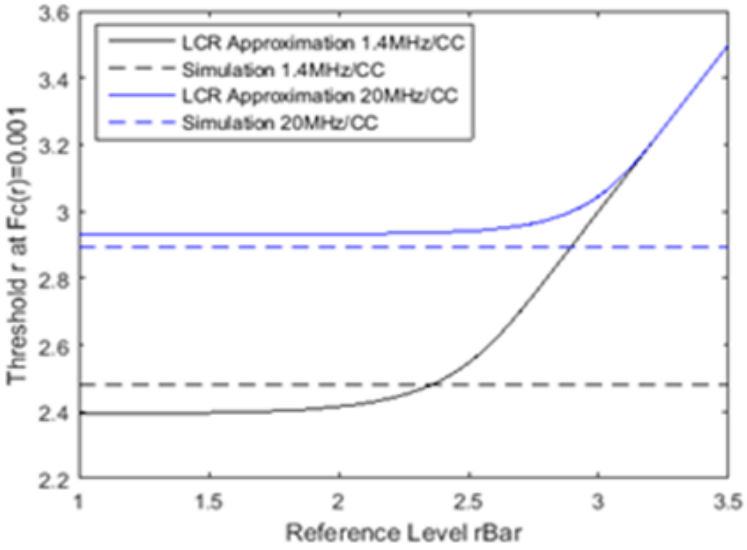

Figure 3.2: r vs $\bar{r}$ for Contiguous CA-OFDM, with CC=2

Similar to [1], the effect of the level $\bar{r}$ is first studied for the mentioned above cases, where $\bar{r}$ is determined by plotting $rvs.\bar{r}$ from the expression at $F_c(r) = 0.001$ along with the simulation value at this target F_c. It follows that $\bar{r}$ is the value where the simulations agree with the expression of $F_c(r)$ at the target point of F_c. Recall that r represents the random variable corresponding to the CF and

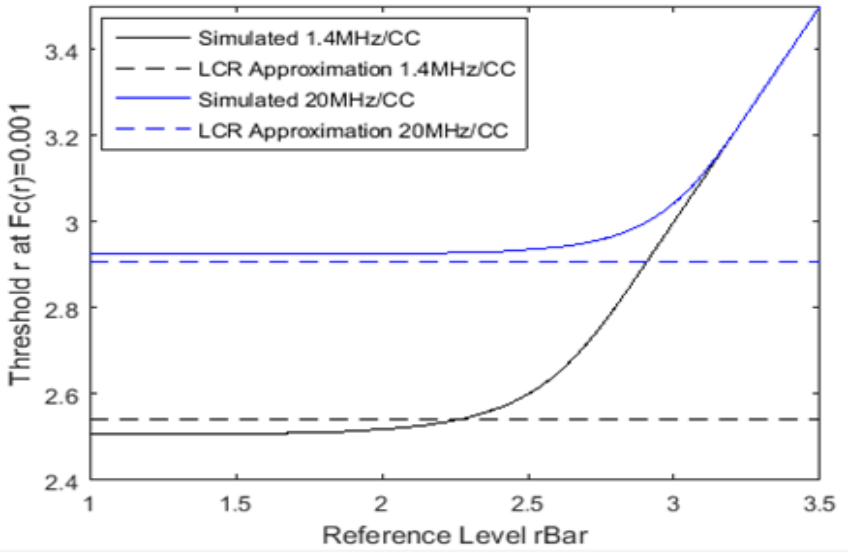

Figure 3.3: r vs $\bar{r}$ for Non-Contiguous CA-OFDM, with CC=2

$\bar{r}$ is the reference threshold level that conditions the CDF of the CF to cross it, inorder to guarantee that each level crossing constitutes a peak.

Figures 3.2 and 3.3 show $rvs.\bar{r}$ for the contiguous and non-contiguous cases respectively for CC=2. Both figures show good agreement between the analytical expression of $F_c(r)$ and the simulation for $\bar{r} \in [1.7 : 2.4]$. In order to be consistent with the results of [1], $\bar{r}$ will be chosen to be $\sqrt{\pi}$ in the subsequent CDF plots.

3.5.2 Cumulative Distribution of the Crest Factor

Figure 3.4 and Figure 3.5 show the CDFs of the CF of 3.26 with $\bar{r} = \sqrt{\pi}$ against the simulation results for the contiguous and non-contiguous aggregation respectively.

It can be seen from the below figures that the simulation shows good agreement with the proposed expression, and the simulation better agrees with the expression as the bandwidth is increased since the discrepancies observed for the 1.4MHz/CC case between the proposed expression and the simulation for the contiguous case are due to the fact that the Gaussian approximation is not accurate enough for the CLT to hold. This is because to allocate a bandwidth of 1.4MHz/CC to each user, 6 Resource Blocks (RB) are assigned, while 100RBs are needed to allocate a 100MHz bandwidth per CC. So the larger the bandwidth is, more elements will be summed up in the time domain. Also, Figures 3.4 and 3.5 show that the expression is more accurate for the non-contiguous aggregation. This can be interpreted as follows: for the contiguous aggregation with 1.4MHz/CC, from 3.24, the average level crossing rate $({v^+}_c)$ per T_s is found

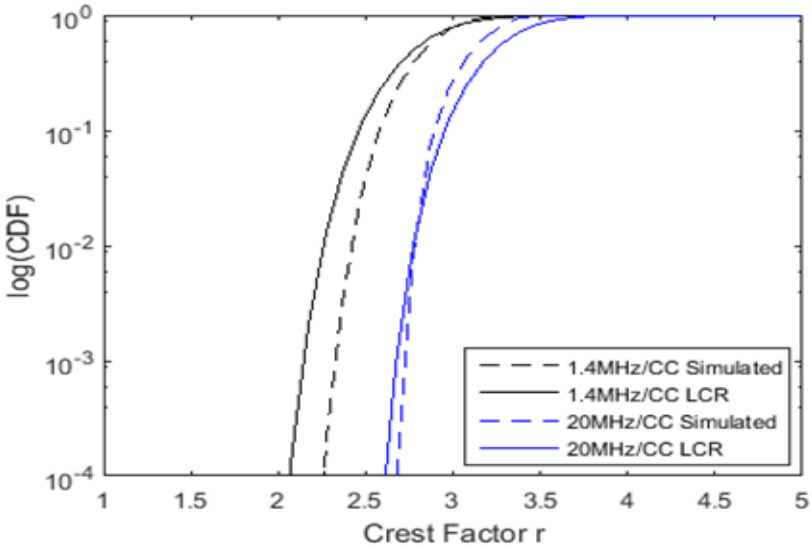

Figure 3.4: Comparison of the analytical CF Distribution of CA-OFDM with the simulation results for contiguous aggregation, CC=2

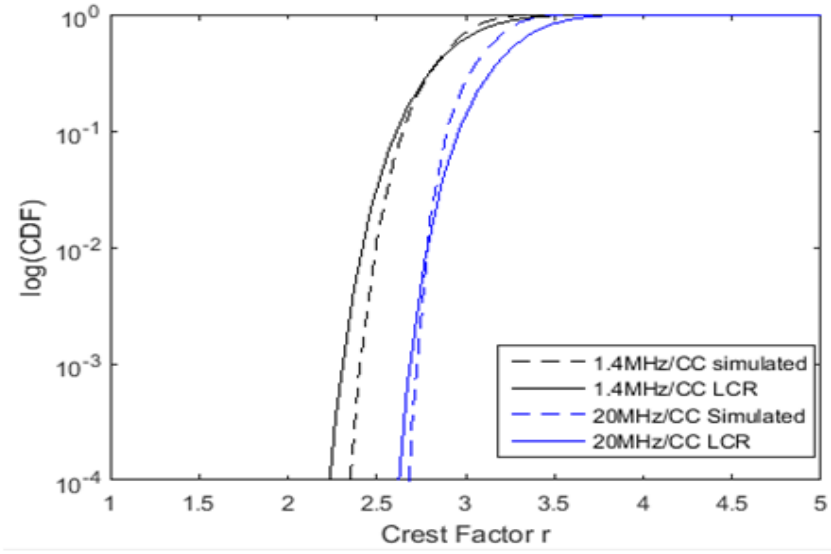

Figure 3.5: Comparison of the analytical CF Distribution of CA-OFDM with the simulation results for Non-contiguous aggregation, CC=2

to be 5.5869×10^5 crossings per one CA-OFDM symbol period. This gives an average number of peaks equals to 37.2459. However in the non-contiguous case for the same bandwidth, ${v^+}_{c,Agg}$ is found to be 1.2779×10^6 crossings per one

CA-OFDM symbol period and a mean number of peaks equals to 85.1955. Thus the expression detects the increase in the number of peaks due to the increase in gap size.

3.5.3 Results for CC=5

We also performed simulations to derive experimental results for the scenario of 5 CCs and uniform spacing of 3MHz between the CCs. The results are illustrated in 3.6, where we see consistent results with those of the two component-carriers configuration, although there is a slightly larger gap between the experimental values and analytical values as the CDF tends to 1. However, the expression still shows the increase in the number of peaks as the bandwidth increases (425 peaks in 1.4MHz/CC, and 2416 peaks in 20MHz/CC in one CA-OFDM symbol period).

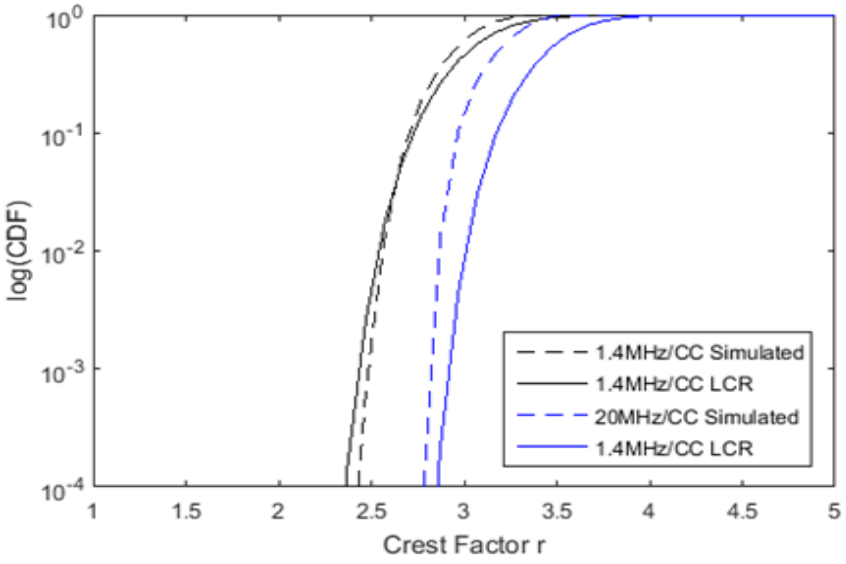

Figure 3.6: Comparison of the analytical CF Distribution of CA-OFDM with the simulation results for Non-contiguous aggregation, CC=5

3.6 Applications and Scenarios

In this section, we focus on PAPR reduction to illustrate the application of our developed PAPR probability distribution in assessing reduction techniques. Chapter 4 will provide extensive and detailed analysis on PAPR reduction. We apply a well-known reduction technique, known as Selective Mapping Technique (SLM) [21], which is based on the notion of generating M-independent candidate signals

through applying M-phase rotations and then choosing the version of aggregated signal that has the minimum PAPR for transmission. We obtain the expression of the Crest Factor (CF) distribution of the signal after applying SLM from the derived expression for the CF distribution of the original aggregated signal for the case of CC=2. The expression of the CDF of the signal after applying SLM is approximated simply by raising equation(3.26) to the power M [22]. We hence have equation 3.31:

$$F_c(r) \approx F_c(r|C > \overline{r}) = (\left(1 - \frac{re^{-r^2}}{\overline{r}e^{-\overline{r}^2}}\right)^{T_S \sqrt{\frac{\frac{4\pi^2}{3}w_1^2 + 4\pi^2 K_1 + 4\pi^2 w_2 \sqrt{K_1} + 4\pi^2 w_2^2}{\pi}} \overline{r}e^{-\overline{r}^2}})^M \tag{3.31}$$

For proof of concept, we simulated a non-contiguous signal with bandwidth per

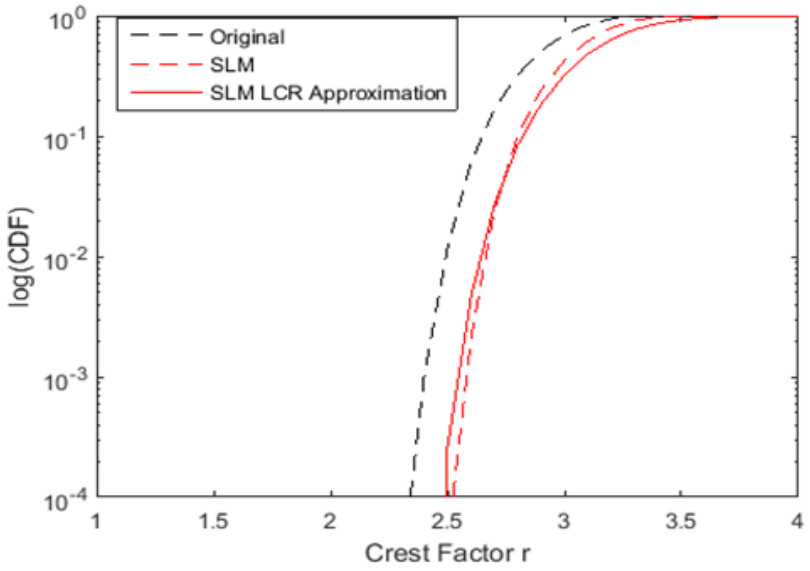

Figure 3.7: Comparison of the analytical CF Distribution of CA-OFDM with the simulation results after applying SLM for CC=2

CC equals to 1.4MHz and similar configuration to the previous simulations, with a number of candidate signals M equals to 3. Figure 3.7 shows the effect of SLM on the signal envelope peak distribution. Also, the analytical expression appears to be in very good agreement with the simulations. From Figure 3.8, SLM achieves PAPR reduction of approximately 1dB.

3.7 Chapter conclusion

In this chapter, we provided a literature review and discussion about PAPR distribution analysis techniques in OFDM systems. Since no similar work was done

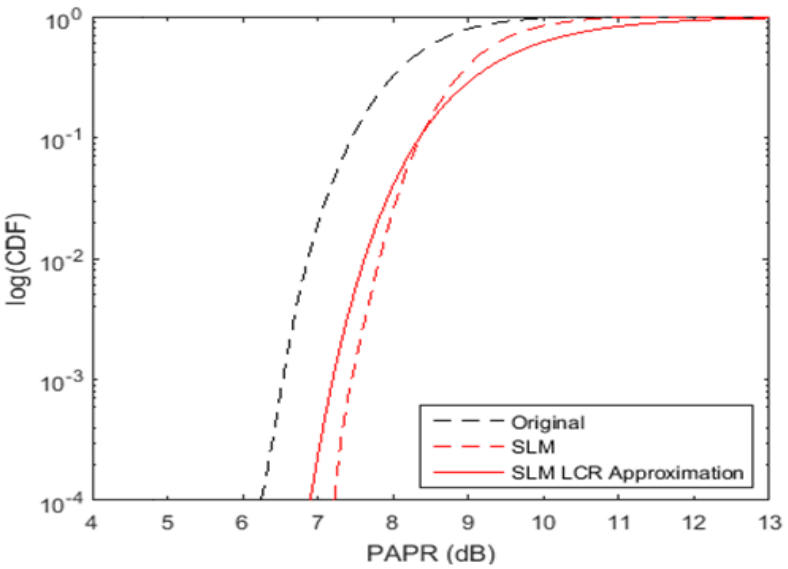

Figure 3.8: Comparison of the analytical PAPR Distribution of CA-OFDM with the simulation results after applying SLM for CC=2

to carrier aggregated OFDM systems, we filled this gap in literature by developing a general expression for the distribution of the PAPR of carrier aggregated OFDM signals by approximating the CDF of the crest factor of the signal, using Level Crossing Rate (LCR) analysis.

This approach allows us to approximate the number of peaks by the number of upward crossings to a certain reference threshold level. The accuracy of the expression was verified against simulations for contiguous and non-contiguous aggregation schemes for the minimal and maximal bandwidths, as stated in the standards of LTE Release 8. The approximation depends on the allocated bandwidth of the signal and on the component carrier spacing among the CCs.

The distribution of the PAPR is crucial in the performance evaluation of PAPR reduction techniques, and to show this, we modeled the reduction capability of the SLM scheme by using the derived model, where good accuracy was demonstrated against the simulations. In the next chapter, we analyze PAPR reduction techniques and propose a new PAPR reduction technique referred to as Peak Valley Alignment.

Chapter 4

PAPR Reduction in CA-OFDM Systems

4.1 Chapter Introduction

In the previous chapter we provided a detailed discussion about PAPR Analysis. In this chapter we shed the light on PAPR reduction techniques. Then we propose and analyze a new PAPR reduction technique for CA-OFDM systems. Figure 4.1 shows the transmitter architecture of the carrier aggregated system that we adopt. Intuitively, a possible solution to the PAPR problem would be reducing the signal peak power by backing off the input power; however this is not an efficient solution as it decreases the efficiency of the system, as we will show in 6. Thus the PAPR problem should be tackled in a way that does not decrease the power efficiency. This complicates the design of an efficient power amplifier with high linearity.

The PAPR problem appeared since the early applications of OFDM systems. Indeed, much research was done to tackle it from different perspectives, ranging from analyzing the PAPR distribution as discussed in the previous chapter to proposing countless techniques for PAPR reduction [23]. These techniques include and are not limited to tone reservation, active constellation extension, selective mapping (SLM) which is based on the notion of generating M-independent candidate signals through applying M-phase rotations and then choosing the version of signal that has the minimum PAPR for transmission, coding techniques, etc.

When LTE Advanced (LTE-A) was released with the feature of carrier aggregation, the PAPR problem escalated along with the new release, as the aggregation of multiple OFDM and even multiple SC-FDMA signals, led to severe increases again in the PAPR of the signals. Thus, more research was made to address the PAPR problem within the carrier aggregation context.

It can be seen that as carrier aggregation of OFDM and SCFDMA signals

continue to evolve, the PAPR problem will persist but with additional challenges. These challenges appear in the form of the need for reduction techniques that are high performing, but at the same time are computationaly less, regardless of the increase in the number of component carriers that are aggregated together.

Toward meeting this need, we propose in this chapter a new PAPR reduction technique for carrier aggregated OFDM systems which we refer to as Peak Valley Alignment (PVA), while building on some of the results in [2]. Note that the application of the derived expression of the PAPR probability distribution to SLM was straight forward since the candidate signals are independent [2], hence the PAPR distribution of the SLM processed signal is simply the obtained expression raised to the power of the number of candidate signals.

However as will be explained within this chapter, the independence among the candidate signals does not hold anymore, and modeling the dependencies among the component carriers, complicates the analysis. For the sake of space, we do not include in this chapter the expressions derived previously in [2].

Our contributions through the proposed Peak Valley Alignment can be summarized as follows:

- Presenting a distortion-less technique that offers superior PAPR reduction gains compared to existing hueristic techniques, and can achieve close performance to optimization-based techniques.

- Demonstrating the increase in coverage area gain due to reducing the PAPR.

- Deriving the computational complexity of PVA and showing that it offers a significant reduction in computational complexity relative to existing techniques, which appears when increasing the number of aggregated component carriers.

4.2 Literature Review and Discussion

In this section, we provide a literature overview for some of the works that proposed PAPR reduction techniques for CA-OFDM and CA-SCFDMA systems. Then we compare them with respect to some parameters and the methodologies used. In a manner similar to typical OFDM systems, PAPR reduction techniques fall broadly under two categories: Distortion-based and distortion-less techniques.

The former category reduces the PAPR at the cost of in-band and out-of-band distortion. This leads to an erroneous reception of the data unless additional error mitigation is made at the receiver, which induces additional complexities. Some of these techniques are clipping and filtering [24], where it is a simple non-linear operation that clips the signal envelope samples that exceed a certain threshold.

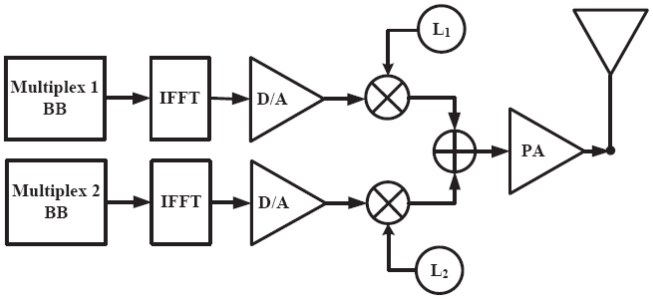

Figure 4.1: Transmitter Architecture for CA with two component carriers.

The second broad category can be termed as multiple signaling and probabilistic techniques [23], which either produce multiple versions of the signal then select the version with the lowest PAPR for transmission, or they introduce peak reducing signals that are customized to reduce the signal peaks upon addition. The Multiple signaling approaches are in turn divided into processing the signal in frequency domain [25], and in time domain [26][27]. The frequency domain approaches apply phase shifts to the modulated subcarriers prior to IFFT, but this comes at the cost of having to perform an IFFT for every candidate signal. Partial Selective Mapping (PSLM) [25] reduces the complexity of selective mapping (SLM)[21] , which is a frequency domain-based technique, by dividing the subcarriers of each CC into groups and multiplying a small number of these groups by vectors of phases of size H thus resulting in H candidate signals to be tested. The signal with the smallest PAPR is then chosen for transmission.

On the contrary, time domain processing is done by employing a set of circular shifts after the IFFT block, thus eliminating the need for multiple IFFTs. In [26], the proposed technique applies incremental circular shifts across each i^{th} CC, with $i > 1$ and a step size equal to the number of discrete time samples in each partition. Each CC_i is partitioned into Q subsets which results in $V = Q^{CC_{nb}-1}$ different versions of the same aggregated signal. It is referred as "Circular Shift Partition" technique.

In [28] the authors proposed a combined method of frequency domain spectrum shaping using a RRC filter and post-IFFT time domain random phase rotation using a set of phase masks, such as {-1, -j, 1, j} with different iterations, and the signal with minimum PAPR and corresponding phase sequence are transmitted.

The aforementioned approaches can be classified as heuristic techniques, which are known to solve the problem faster and more efficiently than traditional methods by sacrificing optimality, accuracy, precision, or completeness. They are most often employed when approximate solutions are sufficient and exact solutions are computationally expensive.

Other works approached the problem systematically, seeking deterministic and optimal results. We provide and discuss some of them. In [29], the authors exploit the relation between the PAPR and the auto correlation of the data sequence. They propose to reduce the PAPR of the signal by decorrelating the input data sequence using the KLT transform. Compared to other decorrelation algorithms, KLT is optimal in the sense that it perfectly de-correlates the signal and thus has optimal PAPR performance. However KLT is signal dependent and changes from one signal to another. Thus for every transformed signal of size N, all N^2 transform coefficients used in the transform matrix of size $N \times N$ shall be transmitted to the receiver to allow for perfect signal recovery. To overcome this problem, the proposed technique reduces the size of the precoding matrix, by treating each CC signal as a separate random variable so that it becomes small and practical, allowing the KLT based algorithm to be realizable in practical systems. In short, it showed a fixed PAPR reduction capability, with a corresponding fixed complexity. So, to use this technique, the available resources should be able to support its complexity and hence it can be used for delay tolerant applications. Besides, this technique does not support backward compatibility with LTE release 8.

On another hand, [30] tackled the PAPR problem by applying tone reservation in an optimization-driven manner. In their work, they used Second Order Cone Programming (SOCP) to compute the values to be held by the Peak Reducing Signals (PRS) and called their method TR-SOCP. One of their test cases for TR-SOCP is a dual band OFDM signal, which can be seen as a carrier aggregated OFDM signal with 2 CCs. Their approach is distortion-less and gives optimal PAPR reduction gain, however it comes at the cost of very high complexity due to the $L\infty$-minimization, and violates power mask constraints. The power mask problem was then solved by adding power constraints on the peak reducing signal, but the PAPR reduction gain decreases drastically, so that it fails the complexity-performance trade-off.

Finally, it is worth mentioning the work done in [27], where stochastic optimization, namely simulated annealing was used to reduce the PAPR. This approach is considered a metaheuristic approach that can find good solutions with less computational effort than optimization algorithms, iterative methods, or simple heuristics.

In this chapter, we select [25] and [26] as the heuristic multiple signaling techniques that our proposed PAPR reduction technique is compared to, and for the systematic approach, we choose [30] as a baseline method.

4.3 Proposed Peak Valley Alignment

The proposed technique builds on the concept used in the peak cancellation PAPR reduction technique in [31] for non-aggregated OFDM, where the peaks that

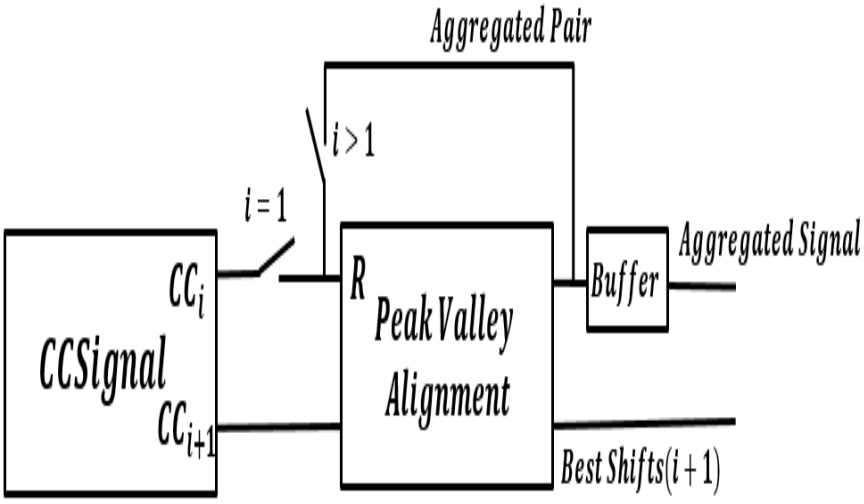

Figure 4.2: Block Diagram of PVA.

exceed a certain threshold are detected and reduced with the help of generated peak cancellation waveforms. However, such an approach degrades the BER performance at the receiver, which is never desirable in practical communications systems. In our technique, we align the extracted peaks and valleys of the different CCs, by applying a set of candidate circular shifts $\{r_i\}$ after the IFFT block.The resulting aggregated OFDM signal is given by

$$s_{Agg}[n] = \sum_{j=1}^{CC_{nb}} s_j[(n - r_i)_N] \tag{4.1}$$

where $(.)_N$ corresponds to the modulus operator with respect to N. In order to maintain backward compatibility with LTE Release 8, we keep the initial CC ($i = 0$) intact without applying any circular shift e.g. $r_0 = 0$. The corresponding PAPR of the aggregated OFDM signal in Equation (4.1) can be reduced in an optimal manner by searching for the best circular shift vector $R^*_{best} = [r^*_1 r^*_2 ... r^*_{CC_{nb-1}}]$ as follows:

$$R^*_{best} = \text{argmin}_R PAPR(S_{Agg}[n]) \tag{4.2}$$

Equation (4.2) requires searching $N^{CC_{nb}-1}$ combinations of circular shift vectors each of size $CC_{nb} - 1$. As mentioned in the previous section, although [26] achieved good PAPR reduction performance, it suffers from an increase in complexity and processing time when increasing the number of CCs. Thus in order to overcome this limitation, in the proposed technique, we reduce the number of circular shifts to be tested by generating a reduced set of circular shift vectors

that can achieve optimal or near-optimal PAPR reduction performance. The aggregated OFDM signal in Equation (4.1) is a complex signal composed of real and imaginary parts and can be expanded into the following expression:

$$\begin{aligned} S_{Agg}[n] &= Real(S_{Agg}[n]) + jImag(S_{Agg}[n])) \\ &= \sum_{i=1}^{CC_{nb}} Real(s_i[(n-r_i)_N]) + j\sum_{i=1}^{CC_{nb}} Imag(s_i[(n-r_i)_N]) \end{aligned} \quad (4.3)$$

It is clear from equation (4.3) that each of the real parts and the imaginary parts of the signals of the CCs are aggregated together. Hence in order to reduce the complexity burden, either the real or the imaginary part is processed as usually done in the active constellation extension PAPR reduction technique to simplify the processing [23].

In our simulation, we choose to process the real part of the signals. The idea of Peak Valley Alignment is inspired from the sequence alignment techniques that are used in bioinformatics. They are based on dynamic programming to determine the optimal alignment between the desired sequences. However, most of such techniques use heuristic methods rather than the global alignment algorithm because identifying the optimal alignment among multiple sequences of moderate lengths is prohibitively computationally expensive. An example of such techniques is the Needleman-Wunsch algorithm [32].

In this work, we use a heuristic sequence alignment technique to align the set of peaks and valleys coming from different CCs. This technique is characterized by its low computational complexity as compared to other heuristic techniques proposed in the literature, and is capable of detecting circular shifts which aligns the considered pair of sequences. The proposed recursive algorithm consists of several phases described as follows:

Phase1: Signal Pair Selection: Initially, the first CC is set as a reference signal and is fed as an input along with the second CC to the PVA block. After applying the steps to be described in what follows, the new reference becomes the aggregated input signal pair, and the next CC from the remaining ones is then supplied to the PVA block, and so on. Figure 4.2 is a flow diagram that describes the recursive algorithm of our technique.

Phase2: Peaks and Valleys Selection: In this phase, we define the peaks and valleys of interest based on a threshold that depends on the characteristics of the signal itself, and is thus adaptive to the variations in the signal. Initially, we split the real part of the i^{th} and $(i+1)^{th}$CC into positive and negative samples. where the former corresponds to the overall set of positive samples while the latter corresponds to the total set of negative samples. We let ${P^+}_i = \{{P^+}_{i,0}, {P^+}_{i,1}, {P^+}_{i,2}, ...{P^+}_{i,N_{peaks}-1}\}$ denote the samples defined as the positive discrete samples of a real signal CC_i with a total number of elements equal to N_{pos} and with mean $\mu_i^+ = E[P_i^+]$. The positions corresponding to these

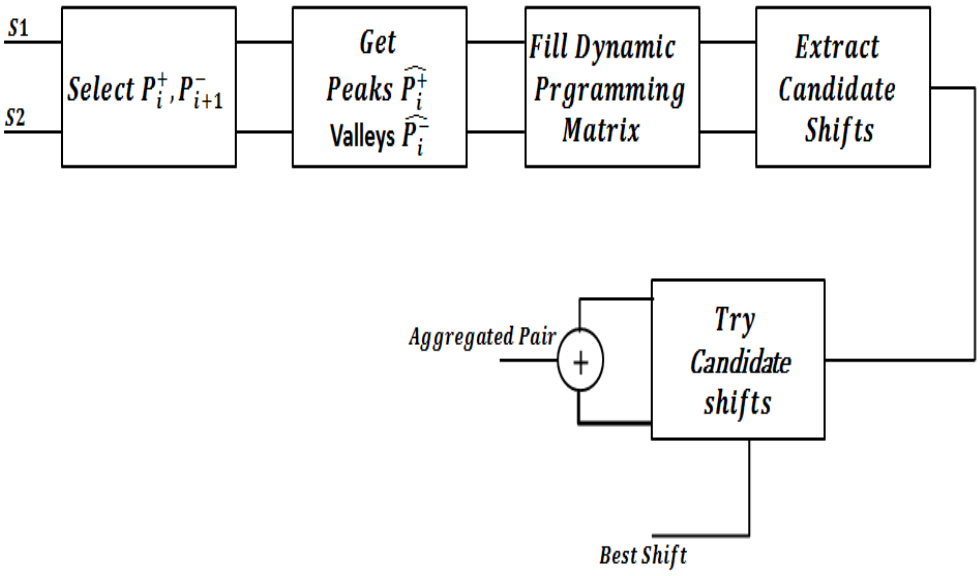

Figure 4.3: Block Diagram of PVA.

samples are defined $Pos^+{}_i = \{Pos^+_{i,0}, Pos^+_{i,1}, Pos^+_{i,2}, ...Pos^+_{i,N_{peaks-1}}\}$. In a similar manner, we define the total set of the negative discrete time samples of a real signal of the $(i+1)^{th}$ CC as $P^-{}_{i+1} = \{P^-{}_{i+1,0}, P^-_{i+1,1}, P^-_{i+1,2}, ...P^-_{i+1,N_{val-1}}\}$ with a total number of elements equals to N_{neg}, $\mu^-_{i+1} = E[P^-_{i+1}]$ and corresponding positions defined as $Pos^-{}_{i+1} = \{Pos^-_{i+1,0}, Pos^-_{i+1,1}, Pos^-_{i+1,2}, ...Pos^-_{i+1,N_{val-1}}\}$. Then from each set $P^+{}_i$ and $P^-{}_{i+1}$, we define $\hat{P}^+{}_i$ and $\hat{P}^-{}_{i+1}$ as the respective selected peaks of size N_{peaks} and valleys of size N_{val} whose amplitudes obey the threshold conditions $Thresh^+$ and $Thresh^-$ respectively. We let $\hat{Pos}^+_i$ and $\hat{Pos}^-_{i+1}$ denote their respective positions. In [2], we derived an approximation of the distribution of PAPR for CA-OFDM signals. In the derivation, we obtain an expression for the average number of peaks, which is equal to the number of upward crossings to a certain reference level within the OFDM symbol period. As will be explained in the simulation results, the thresholds ($Thresh^+$ and $Thresh^-$) are adjusted to yield a number of peaks and valleys respectively, that matches the theoretical average number of peaks/valleys in the signal.

Phase3:Circular Shifts Using Pairwise Alignment Algorithm: Based on the selected peaks and valleys from the pair being under process, we are interested in the circular shift that aligns the set of selected peaks $\hat{P}_i{}^+$ of the reference signal with the set of the selected valleys $\hat{P}^-_{i+1}$ of the consecutive CC. The optimal alignment can be achieved by using the Needleman-Wunsch algorithm [32]. This algorithm is based on dynamic programming and uses the edit distance (a mea-

sure of difference) concept that accounts for the score of matches, mismatches and gap insertion when aligning one sequence to another.

When searching for alignment between pair of sequences, the best circular shift is the one that maximizes the matching score between the two sequences. However, the processing required for the calculation of the score for every possible circular shift has a computational complexity of $N \times L \times N_{peaks} \times N_{val}$ which makes it impractical. Not to mention also that the Needleman-Wunsch algorithm inserts gaps within the aligned sequence pairs, which is in-feasible in our context of dealing with communications signals. Thus, as an alternative, we rely on a simple and fast heuristic technique [33], where instead of searching for a single optimal circular shift, it detects the possible circular shifts between the aligned sequence pairs.

In the bioinformatics context, the method aims to detect naturally occurring circular shifts within protein sequences. Our developed algorithm differs from the Needleman-Wunsch algorithm in two steps. The first is comparing the first sequence to a duplication of the second sequence, so in our case the set $\hat{Pos}_i^+$ is compared against $\{\hat{Pos}_{i+1}^-, \hat{Pos}_{i+1}^-\}$. The second is in the initialization of the first column of the dynamic programming matrix, as will be illustrated. The steps of the algorithm can be described as follows:

1. Initialize the first row of the dynamic programming matrix with 0s and the first column with $0...N_{peaks}$.

2. Fill up the dynamic programming matrix $D(u, v)$ recursively using the following recurrence equation:

$$D(u,v) = max \begin{cases} D(u-1, v-1) + T(u,v) \\ D(u-1, v) + w \\ D(u, v-1) + w \\ 0 \end{cases} \tag{4.4}$$

   Where $T(u, v) = 1$ in case of a match or -1 in case of a mismatch between the samples corresponding to $\hat{Pos}_i^+$ and $\hat{Pos}_{i+1}^-$.The parameter w corresponds to the gap penalty and is chosen to be -1 in our case. Note that zero is selected when the first three options are negative.

3. Select all possible candidate circular shifts by back tracing, starting from the elements with best scores in the bottom row of the matrix until a zero is reached. This is equivalent to selecting zero positions in the left half of the matrix excluding those in the first row ($u = 0$) and those in the first column ($v = 0$), then computing the corresponding circular shift (cs) is as follows:

$$cs = u - v \ \forall \ D(u,v) = 0 \mid 0 < u < N_{peaks}, 0 < v < N_{val} \tag{4.5}$$

In figure 4.3, we show a diagram corresponding to the inner structure of the PVA block, that describes this phase.

Phase4: Aligning Pairs of sequences: In this phase, the candidate shift vector that resulted from the current pair of signals is tested for each shift and the corresponding PAPR is calculated. Then CC_{i+1} is shifted by the best shift, and finally the reference signal is set to be the new aggregated signal, i.e., $ref = ref + CC_{i+1}$, and the steps are repeated until all the CCs are processed. The vector corresponding to the circular shifts for the component carriers is sent as side information for recovery at the receiver. The receiver multiplies the output of the FFT block by $e^{j2\pi\frac{kr}{N}}$ with $k = 0, 1, ...N-1$ based on the circular shift property of the DFT [34].

Finally, in regards to the overhead required by PVA, it was indicated in [26] that using the Reference Signals to send the side information reduces the burden of the added side information. Thus the same procedure is applied here.

4.4 Simulation Results

In this section we present the simulation results of the proposed peak valley alignment, and compare it to the heuristic techniques PSLM [25] and the random circular shifts [26] on one side, and to the optimization based systematic technique TR-SOCP [30] on the other hand. The aim from this comparison is to establish a complexity-performance trade-off between heuristic and systematic PAPR reduction. We show that the performance achieved by systematic methods can be approximately achieved with much lower complexity by using heuristics.

The PAPR performance of the methods are studied by plotting the CCDF functions of PAPR along with the improvement of area of coverage due to PAPR reduction. [35] indicated that relying only on the CCDF for evaluating the performance of a certain PAPR reduction technique is not sufficient. This is because CCDF, which gives the distribution of the PAPR before the HPA, fails to take into account what happens to the signal after it passes through the HPA. Thus for a practical assessment of the system, a more important and convenient metric should be considered. This metric is referred to as the MER (Modulation Error Ratio) or the EVM (Error Vector Magnitude), which are by some means are interchangeable.

A signal sent by an ideal transmitter or received by a receiver would have all constellation points precisely at the ideal locations, however various imperfections in the implementation such as the distortion caused by the HPA, cause the actual constellation points to deviate from the ideal locations. The MER therefore is a comparison of the actual location of a received symbol to its ideal location. It is

Table 4.1: Theoretical Average Number of Peaks and Valleys

CC_{nb}	Avg. $N_{PeaksTheo}$ / $N_{valTheo}$
2	47
3	93
4	168
5	240

defined as [35]:

$$\mathrm{MER}\{\mathbf{X}, \widehat{\mathbf{X}}\} = 10 \log_{10} \left(\frac{\|\mathbf{X}\|_2^2}{\|\mathbf{X} - \widehat{\mathbf{X}}\|_2^2} \right) \tag{4.6}$$

where $\mathbf{X}$ is the ideal symbol vector measured at the input of the amplifier and is measured at the output of the HPA. In this thesis, we start the analysis in this chapter in terms of the CCDf and proceed in chapter 6 to analyze the MER/EVM metrics.

Next, the BER of the peak valley alignment method is compared to that of the original CA-OFDM signal. Finally, we provide a complexity analysis comparison among the above techniques, to demonstrate the significant complexity reduction offered by our proposed technique. The advantage of our method is more significant as the number of CCs increase beyond two. For our simulation, we implement a contiguous carrier aggregation scheme where each CC has a bandwidth of 1.4MHz. As indicated in the standard of LTE release 8, this bandwidth corresponds to an IFFT size of $N = 128$, $d = 72$ user data subcarriers, and with an oversampling factor of $L = 2CC_{nb}$. The modulation scheme used is 16 QAM. As for the thresholds $Thres^+$ and $Thres^-$, Table 4.1 provides the average number of peaks and valleys to be extracted for each number of CCs. Note that our expression of average number of peaks in [**7**], approximates the number of peaks by counting the upward crossings of a certain threshold reference level. Similarly, the number of valleys can be approximated by counting the downward crossings of a certain threshold. It follows that it is valid to assume that the peaks and valleys follow the same distribution. Since the value of the threshold depends on the signal, we base it on the mean and the variance of the real or imaginary part of the sets of positive and negative discrete samples (P_i^+ and P_{i+1}^-) respectively. The expression of the average number of peaks shows that the peaks constitute around 10-to-20 % of the signal. Thus, in our case we process a small portion of the samples to reduce the PAPR, as we will describe in details in the complexity analysis section.

4.4.1 PAPR Performamce

To show the improvement in PAPR reduction gain offered by PVA against the hueristic methods [25][26] we are comparing against, we adopt the parameters

used there in. For PSLM, we divide each CC into 6 groups and apply a phase

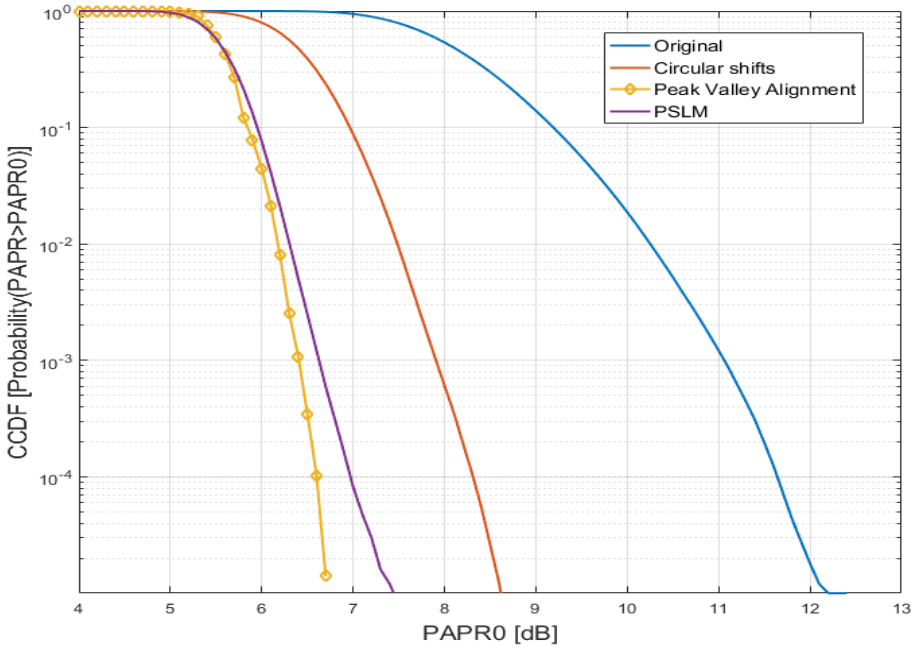

Figure 4.4: CCDF of PAPR for PVA against the other hueristic methods.

rotation for the last four groups, with phase values 0 and π. It was shown in [25] that applying the phase rotations to the last 4 groups gives a better PAPR reduction performance. On the other hand, for the circular shifts partitions, we set the partition number Q to be 8. Finally for the TR-SOCP method, we use the MB-OFDM signal used in [30], meaning that we simulate a dual band ofdm signal, with N-IFFT size of 64, including 48 data subcarriers and 6 resereved subcarriers per each CC to act as the peak reducing signal. Figure 4.4 shows the PAPR reduction performance of PVA in comparison to PSLM and circular shifts partitioning, for the case of two component carriers. It can be seen that Peak Valley Alignment achieves a slightly better PAPR reduction gain achieved by PSLM (<1dB gain), but at a much lower cost as will be explained in the complexity analysis sub section. At a probability level of 10^{-4}, PVA provides approximately a 5 dB PAPR reduction, whereas circular shifts partitions achieves a 3.3 dB reduction gain. Thus PVA out-performs circular shifts partition by 1.7 dB. Figure 4.5 shows the PAPR CCDFs for the case of 3, 4 and 5 component carriers. It can be seen that the PAPR improves by around 4.5 to 4.7 dBs. It is worth mentioning that according to our testing, the order in which the CCs are aggregated within the recursive algorithm does not change the outcome. This is due to the fact that prior to PVA application, each CC is generated independently following the same probability distribution. Thus the order of CCs when applied into PVA shall not make any difference in PAPR reduction

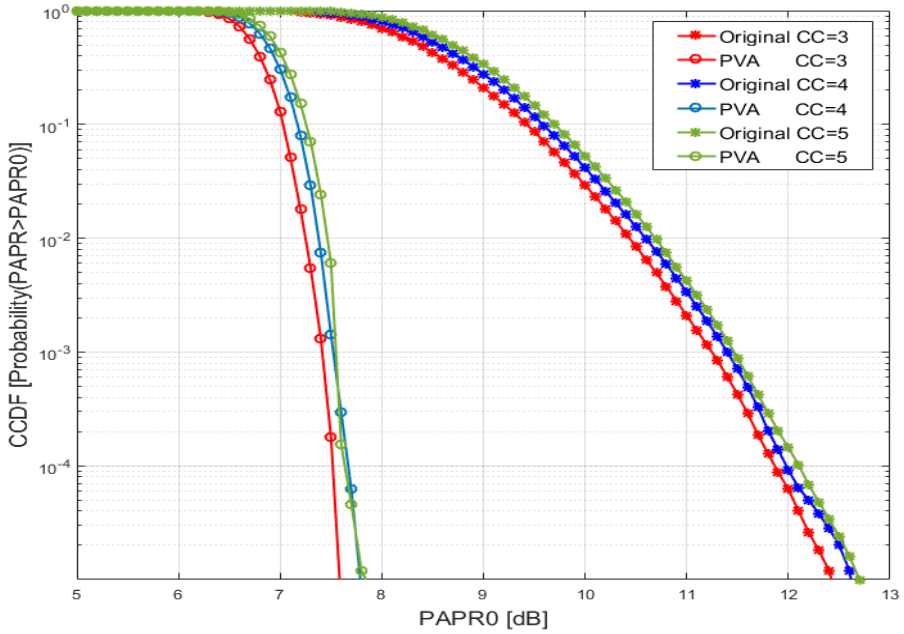

Figure 4.5: CCDF of PAPR for PVA in the case of 3, 4 and 5 CCs.

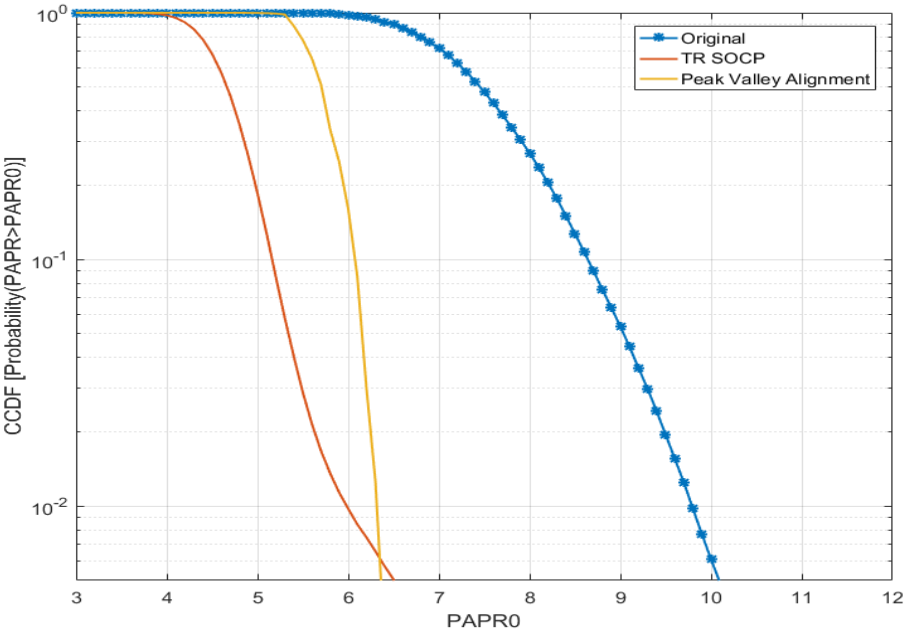

Figure 4.6: CCDF of PAPR for PVA against TR-SOCP.

performance. Furthermore, when comparing PVA against TR-SOCP, it can be

seen from figure 4.6 that PVA achieves a slightly worse performance than the implemented TR-SOCP.

4.4.2 BER Analysis

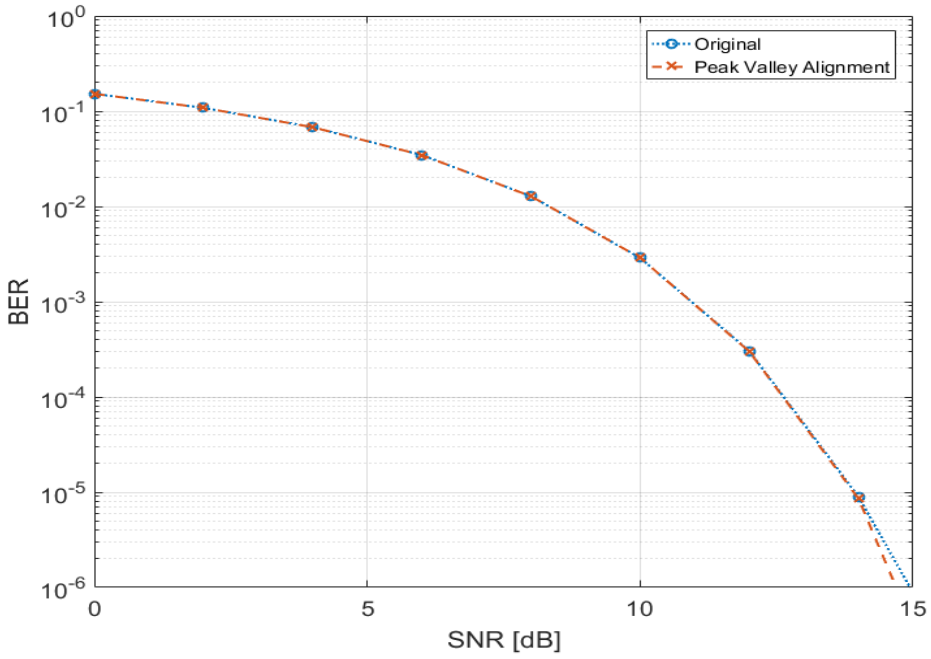

Figure 4.7: BER vs. SNR plot of PVA and the original CA-OFDM Signal.

Since our method concerns the transmitter, we assume non-erronous side information transmission, and we simulate an AWGN channel to study the bit error rate at the receiver. Figure 4.7 shows the BER versus SNR plot of the PVA and the original CA-OFDM Signals. It can be seen that PVA is completely distortion-less.

4.4.3 Coverage area Gain

The improvement in the PAPR of the aggregated OFDM signal has a direct implication on the coverage of transmissions in the LTE-A system. A few dBs or even a gain of a small fraction of a dB allows extending the coverage of transmission. The received power at the receiver is related to the distance d between the transmitter and the receiver as well as the power attenuation factor, known as the path-loss exponent β. If we let P_T be the radiated power of the transmitter, then the received power P_R is:

$$P_R = P_T G_T G_R \left(\frac{\theta}{4\pi d}\right)^{\beta} \tag{4.7}$$

where θ corresponds to the wavelength of the radiation and G_T and G_R are the antenna gains of the transmitter and receiver, respectively. In cellular systems modeling, the path loss exponent is assumed to be between 2 and 4, depending on the wireless channel environment. By manipulating Equation 4.7, the distance d can be expressed as

$$d = \frac{\theta}{4\pi}\left(\frac{P_T}{P_R G_T G_R}\right)^{\frac{1}{\beta}} \tag{4.8}$$

The gain in coverage area is then denoted as [36]:

$$\zeta = \frac{\pi d_1^2 - \pi d_0^2}{\pi d_0^2} = \pi\left(\left[\frac{P_{T1}}{P_{T0}}\right]^{\frac{2}{\beta}} - 1\right) \tag{4.9}$$

Where d_0 and P_{T0} are the original range and the original transmit power before

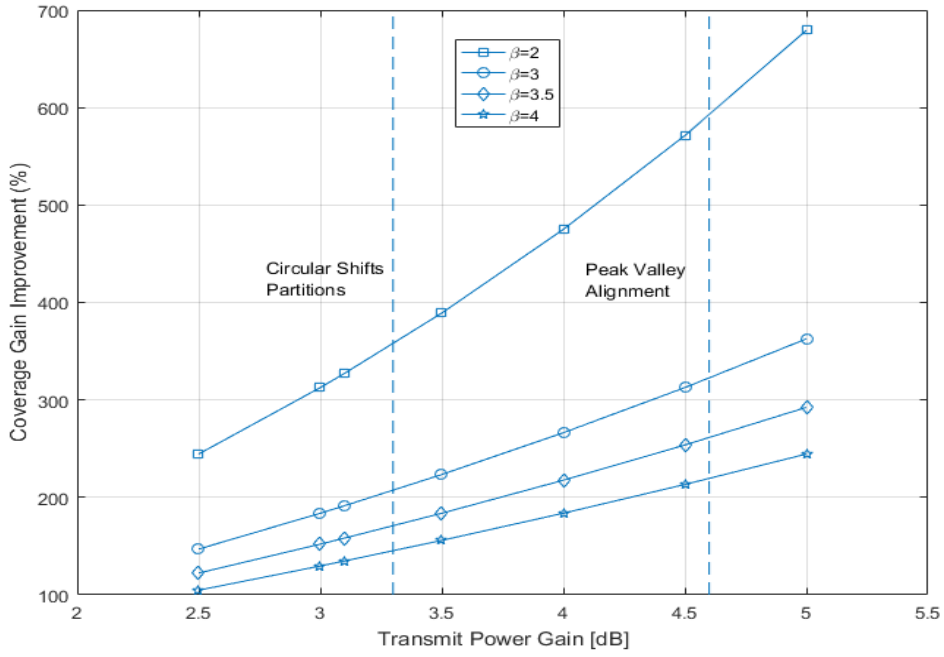

Figure 4.8: Improvement in Coverage Area Gains

PAPR reduction respectively, and d_1 and P_{T1} are the new range and transmit power resulting from the power gain achieved by the PAPR reduction. The relation between the increase in the coverage area and the decrease in PAPR is that reducing PAPR as will be explained in chapter 6, allows to operate closer to saturation thus allowing to increase the transmit power with achieving the same linearity level, therefore remaining within the limits of the power spectral mask. By using the expression in Equation 4.9, we plot the coverage gains achieved by circular shifts partitions and by PVA in figure 4.8. At an average PAPR reduction of 4.6dB, PVA achieves an improvement that ranges from 219% for

Table 4.2: Parameters used for PSLM and Circular Shifts Partitions methods

CC_{nb}	PSLM	Circular Shifts Partition
2	$S = 4, P = 6, H = 256$	$Q = 32$
3	$S = 3, P = 6, H = 512$	$Q = 16$
4	$S = 2, P = 6, H = 256$	$Q = 8$
5	$S = 2, P = 6, H = 1024$	$Q = 8$

$\beta = 4$, to 592.3% for $\beta = 2$. On the other hand, circular shift partitions achieves an improvement range from 145% for $\beta = 4$ to 358% for $\beta = 2$, with a 3.3dB PAPR reduction. Thus PVA increases the coverage gain achieved by circular shifts partitioning by at least 1.5 times, at the same or lower computational complexity. Note that a coverage gain of 100% means that only half of the number of eNodeBs would be required to cover a certain geographical area, and hence large savings in terms of system deployment costs would be realized.

4.4.4 Complexity Analysis

In this sub-section we study the complexity of the proposed peak valley alignment technique at the transmitter and receiver sides, and compare it to that of the PSLM technique of [25] and to that of the circular shift partitioning technique of [26]. In this analysis, we compare the operations required by each technique in terms of real multiplications (RMUL) and real additions (RADD). In addition, we base our analysis on radix-2 decimation in time IFFT implementation, where each IFFT/FFT operation of size N requires $N \log_2(N)$ complex additions and $N/2 \log_2(N)$ complex multiplications [23].This results in $2N \log_2(N)$ RMULs and $3N \log_2(N)$ RADDs for each N-IFFT operation. For the sake of space, we omit the complexity derivations of PSLM and Circular Shifts Partitions.

After analyzing the operations required by each technique, we provide the relative complexity of PVA as compared to PSLM and to circular shifts partitions. For $CC_{nb} = 2, 3, 4$ and 5, We set the parameters of PSLM and circular shifts partitions to achieve the same PAPR performance as that of PVA at probability level of 10^{-4}. The parameters are shown in table 4.2: Recall that in PSLM, phase rotation is applied on S/P groups of the signal, and in circular shifts partitions, Q is the number of partitions of the signal. Furthermore, note that in PVA, each pair of processed signals generates a different number of candidate shifts. Thus we use in the relative complexity calculation the average number of candidate shifts among the 100,000 simulated CA-OFDM symbols.

Complexity of Peak Valley Alignment (PVA): The signals are processed in the time domain, thus only one N-IFFT operation is required for each CC. Thus the complexity is $2CC_{nb}N \log_2(N)$ RMULs and $3CC_{nb}N \log_2(N)$ RADDs. Furthermore, the amplitudes of the time domain OFDM signals of the CCs are compared to a threshold. This comparison requires N RADDs for every

OFDM signal. Thus we have $CC_{nb}N$ RADDs operations. Then the operations in the pairwise alignment, including the dynamic programming matrix filling, and the candidate shifts extractions require $6N_{peaks}N_{val}$ RADDs for each pair of processed signals. This results in a total of $6 \times N_{peaks} \times N_{val} \times (CC_{nb} - 1)$ RADDs. If we let v denote the number of candidate shifts per each processed pair of signals, then according to [23], the operations required to do v aggregations and PAPR measurements are $v(2N+1)$ RMULs and $N(1+3v)-v-1$ RADDs. The last step is repeated for all CCs, so that the there is a total of $v(CC_{nb}-1)$ aggregations and PAPR measurements. This implies that in total, we need $v(2N+1)(CC_{nb}-1)$ RMULs and $(N(1+3v)-v-1)(CC_{nb}-1)$ RADDs.
At the receiver, the signal recovery needs $N(CC_{nb}-1)$ complex multiplications in addition to the N-FFT processing which results in $2CC_{nb}N\log_2(N)+4N(CC_{nb}-1)$ RMULs and $3CC_{nb}N\log_2(N)+2N(CC_{nb}-1)$ RADDs. Figure 4.10 plots the

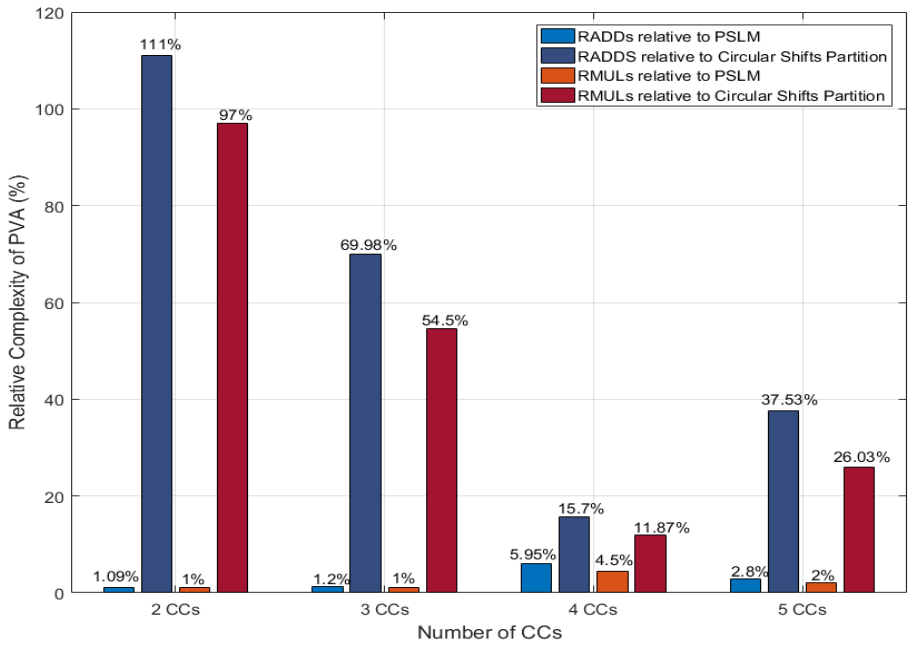

Figure 4.9: % Relative Complexity of PVA w.r.t PSLM and Circular Shifts

relative complexity of PVA with respect to PSLM and Circular Shifts Partitions, in terms of the required relative additions (RADDs) and relative multiplications (RMULs). For the case of 2 CCs, PVA requires around 1% of the RADDs and RMULs that are required by PSLM, and it can be seen that it achieves approximately the same complexity as circular shifts. As the number of CCs increases, PVA maintains an approximately a constant computational complexity relative to PSLM. However, in regards to circular shift partitions, the relative complexity of PVA decreases with the increase in the number of CCs. It should also be noted that the decrease in complexity is not linear with the increase in the number of

CCs. This is because Q is set to 8 in both cases where CCs=4 and CCs=5, so circular shifts partitions tests 512 candidates for CCs=4 and 4096 candidates for CCs=5. For PSLM, it tests 1024 candidates in the case of 5 CCs and tests 256 candidates in the case of 4 CCs, thus resulting in a reduced complexity, while increasing the relative complexity of PVA relative to it. We also compare the complexity of PVA against PSLM and circular shifts partitions for the maximal bandwidth provided by LTE standard. I.e, we compare complexities at a 20MHz bandwidth per CC, for CC=2. The results are similar to those obtained

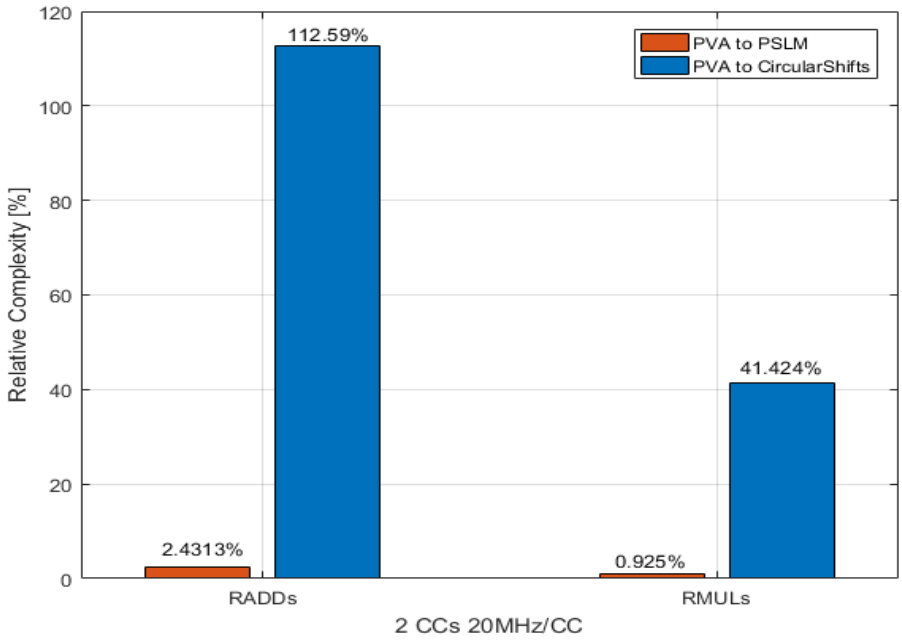

Figure 4.10: % Relative Complexity of PVA w.r.t PSLM and Circular Shifts for a large bandwidth

previously in figure 4.10, where PVA requires respectively 2% and 0.9% of the real additions and real multiplications required by PSLM, and approximately the same percantage of RADDS in comparison to circular shifts partitions, and with 41% of the real multiplications required by circular shifts partitions.

In regards to the complexity of TR-SOCP, it was indicated in [30] that the approximated complexity in TR-SOCP is in the order of $O(NR^2)$, where R is the number of reserved carriers. This is because SOCP is based on the SDPT3 solver, which uses the complex interior point methods to find the optimal solution. We can infer that PVA runs with a significantly lower complexity, while achieving approximately close performance to TR-SOCP.

4.5 Chapter Conclusion

The PAPR problem will remain a serious problem that affects the design of efficient carrier aggregated systems. As more services are being added to current system designs, the need for lower complexity methods that can cope with such designs and lower energy consumptions remains in the spotlight.

This chapter proposed a lower complexity distortionless PAPR reduction technique for carrier aggregated OFDM systems. Its performance was compared against hueristic frequency and time domain processing methods from one side, and against optimization based methods from another side. It was shown through monte-carlo simulations that it has a superior PAPR reduction gain relative to the hueristic techniques, and a close performance to the optimization based technique, in addition to having the advantage of offering a significant reduction in computational complexity.

In the next chapter, we will treat the linearization issue solely. We analyze and apply to our system the famous linearization technique known as Digital Predistortion (DPD). The goal is to provide an independent study of applying DPD only, in order to observe the effects of applying PAPR reduction along side to DPD in 6.

Chapter 5

Linearization of High Power Amplifiers Using Digital Predistortion

5.1 Chapter Introduction

The aim of this chapter is to study and apply Linearization to the system. We choose to apply the good performing and low cost linearization technique known as Digital Predistortion (DPD).

The high power amplifier is a key component in wireless communication systems and its performance sets a bottleneck to the system. As shown in figure 5.1, it consumes more than 50% of the power of the system. It is essentially used in the RF transmitter where a low power input signal needs to be transmitted for long distances. Power amplifiers are classified according to various criteria. Considering the linearity, power ampliers are divided into two categories: nonlinear or linear. The linear power amplifiers are divided into class A, AB or B and are not perfectly linear. The nonlinear power amplifiers are divided into : class C, D, E, F, G, H, S and more. We always have a trade-off between power efficiency and spectral efficiency when designing a power amplifier. The highest linearity is achieved with class A amplifier, yet it has a low power efficiency [37].

On the other hand, power amplifiers are also categorized into two types : TWTA (Traveling-Wave Tube Amplier) and SSPA (SolidState Power Amplier). Each type has its own specifications that make it suitable for certain applications. For example, systems with high microwave frequencies typically employ TWTA while SSPA is used at lower frequency bands. In addition, the larger output power supplied by the TWTA shortens its life because of the heat generated by high voltage. SSPA is more reliable than TWTA and weights less which can be critical for some systems. Saleh model is mostly used to model a TWTA while SSPA can be modeled by Rapp model [38].

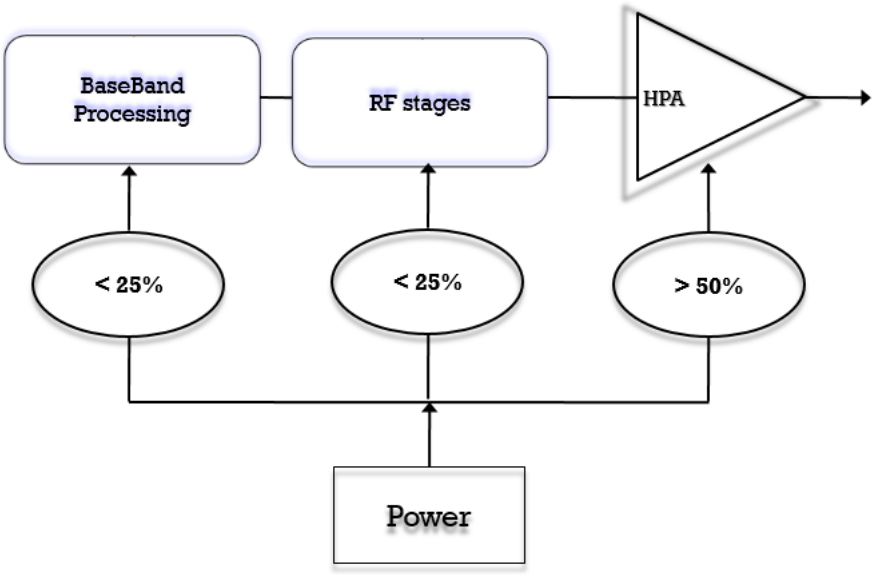

Figure 5.1: Power Consumption in the Transmitter Blocks

Current communication systems mainly use spectrally efficient modulation waveforms, such as orthogonal frequency-division multiplexing (OFDM), that suffer from the high PAPR, which as stated before causes the power amplifier to operate in its non-linear region.

We discuss in this chapter the concept of digital predistortion and then we demonstrate its application on our CA-OFDM system. We show the power spectral density growth into adjacent bands at the output of the HPA, and how the application of DPD suppresses these out of band (OOB) emissions. Then we study the Adjacent Channel Power Ratio (ACPR) performance as a function of the Input Backoff.

5.2 A Summary on Linearization and Digital Predistortion

Linearization of the power amplifier aims to extend its linear behavior into high efficiency regions of operation [39]. Since current cellular base stations require the use of input signals exhibiting both wide bandwidth and large peak-to-average ratios, adaptive digital predistortion is widely used linearization technique to compensate for nonlinearities under such conditions [40].

The predistortion technique consists of adding distortion to the input signal to

eliminate nonlinearity at the output generated by the power amplier. The predistortion linearizer provides the positive amplitude and negative phase deviations for input RF signal to compensate for the nonlinearity of the power amplier. The distortion added by the linearizer usually represents the opposite behavior of the amplitude and phase characteristics of the power amplifier [41].

The operating point of an amplifier without a linearizer must be far from its saturation level because the distortion that exists deep in the nonlinear region is too large to be transmitted. The distance between the operating point and the saturation level is set to be equal to the peak-to-average level of the signal. We will highlight this fact through our simulations in chapter 6.

On the contrary, an amplier with a linearizer can operate at a much higher operating point because the linearizer is able to correct the distortion in the peaks up to the saturation level. It is clear that the pre-distorter cannot correct the distortion beyond the full saturation level of the amplifier. The coefcients of the linearizer are estimated in the digital domain [42]. Thoroughly, DPD is achieved through a two-step process, where first a behavioral modeling is applied to characterize the non-linearities up to the nth order, and then this model is used to estimate and build the inverse characteristic of the PA transfer function. The second step is to apply the estimated inverse function on the input, so that the cascade of the two functions forms an approximately linear process. A simple block diagram of a DPD system is shown in figure 5.2.

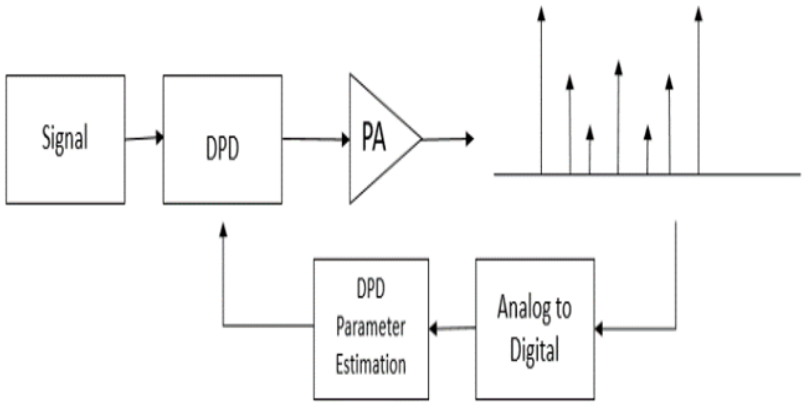

Figure 5.2: DPD system block diagram

Since the predistortion is implemented digitally, it eliminates many challenges present in the analog domain. In other words, it offers a greater degree of precision

for the computation of the predistortion coefficients. Moreover, stability is not an issue in adaptive digital predistortion schemes [40]. It also generates transfer characteristics that would be difficult to implement with discrete components and analog signals. In addition, the cost of applying digital predistortion is relatively low since there is already an allocated power in the digital processor for the signal generation. Adding the predistortion function consists of adding lines of code [43].

Usually, A two metric performance evaluation is usually applied to asses the DPD efciency. The first is a measure of accuracy of the model in estimating the real signal, and is quantied by measuring the Normalized Mean Square Error (NMSE). The other metric is the linearization capability of the Predistorter based on this model. This metric is quantied by measuring the Adjacent Power Channel Ratio (ACPR), i.e., how much power leaks into the other bands as Out of Band Emissions (OOB).

5.2.1 Implementation of DPD

Digital predistortion can be implemented using several techniques. The widely used methods found in the literature are sorted into three main categories : Look-Up Table (LUT) based DPDs, model based DPDs (also called polynomial based DPDs) and neural network based DPDs [38].

1) LUT: The look-up table is a simple method to implement digital predistortion linearization. It consists of recording the amplitude and phase responses of the power amplier as a function of the input power. The signal is then inverted in order to achieve the linearization [44]. The LUT implementation is often static or memoryless limiting the linearization capability and its use in power amplifiers with memory effects [42]. It is simple and easy to implement however it suffers from distortion due to the quantification errors which could be minimized with nonuniform spacing of the look-up table [38].

Mainly, values of the input power versus the magnitude response of the amplifier and versus the phase response are stored in look-up tables. For an input P , the predistorter gets the desired output level from the look-up table. This step may involve a search or the use of a mapping function. The predistorter then applies a correction factor based upon the inverse of the magnitude response. The resulting value is then used to get the phase correction value from the phase table. The nal output is the predistorted sample that should be fed to the amplifier. The look-up table technique depends on varying parameters such as: the size of the look-up table, the algorithm complexity used to calculate the input spacing of the table and the adaptation capability [45].

2) Volterra Series: In wideband applications like OFDM, the operating bandwidth of most system is relatively small with respect to the bandwidth capability of PA hence the memory effects of PA should be considered in predistorter designs [45]. This lead to the implementation of digital pre-distortion

using Volterra series. It is a general nonlinear model that includes dynamics or memory effects. It is represented as:

$$\begin{aligned} y(t) = & \sum_{m_1=0}^{M} h_1(m_1)\, u(t-m_1) \\ & + \sum_{m_1=0}^{M} \sum_{m_2=0}^{M} h_2(m_1, m_2)\, u(t-m_1)\, u(t-m_2) \dots \\ & + \sum_{m_1=0}^{M} \dots \sum_{m_n=0}^{M} h_2(m_1, \dots, m_n)\, u(t-m_1) \dots u(t-m_n) \end{aligned}$$

(5.1)

where the memory depth M is the same for all the polynomial degree. The Volterra series has mixed delays $M \leq m \leq m_1, ... \leq M$ where M is the memory depth. The model gives an accurate representation of the non-linearities however; this is achieved at the cost of high computational complexity due to the fact that as the parameter M increase, a drastic increase in the number of coefcients is needed to compute the model, which results also in complicating the construction of the inverse model of the PA. Thus, this version of VS was used to represent systems with mild non-linearities; and extensive efforts have been made to propose simplications of the VS models that comply with practical systems high non-linearities. For an OFDM input signal, each basis waveform has an effective delay given by $\Delta_{eff} = (m_1 + \ldots + m_p)$. Since some Volterra basis waveforms share the same effective delay, the size of the Volterra basis set could be reduced by mapping one basis waveform for each effective delay and polynomial order p [46]. The number of waveforms in the basis set can be reduced using two processes: pruning [47] [48] or grouping. Some of the well performing techniques are the application of Principle Component Analysis (PCA) [49]or Compressive Sensing (CS) [48] to prune the Volterra series model. These techniques were shown to achieve a similar performance with a noticeable reduction in the computational cost, where CS was shown to achieve a reduction from 400 to 50 coefcients, with negligible performance degradation. Another approach is to modify the model by it-self such as the Memory Polynomial (MP) [50] and Wiener models [51]. The memory polynomial expression is given as [52]:

$$y(t) = \sum_{n=1}^{N} \sum_{m=0}^{M} a_{nm} u(t-\tau_m) \left| u(t-\tau_m) \right|^{n-1} \tag{5.2}$$

where cross-terms are removed in order to simplify calculations while maintaining a reliable and effective solution. However, since cross terms are needed for better

modeling of the delay, Generalized Memory Polynomial (GMP) and Dynamic Deviation Reduction (DDR) have been introduced in [53] and [54]. Another approach is the wiener model which is composed of a cascade of a linear time invariant (LTI) system represented by a linear nite impulse response (FIR) lter, and followed by a memoryless nonlinear system. One major advantage of this model is the possibility to have an exact inverse of the PA. The input output relation of this model is given by [55]:

$$x_{out} = G\left(|x_1(n)|\right) \sum_{j=0}^{M} h(j) x_{in}(n-j) \tag{5.3}$$

where $G\left(|x_1(n)|\right)$ is the memoryless instantaneous gain function, $h(j)$ are the coefcients of the FIR impulse response and M denotes the memory depth. The two blocks undergo system identication sequentially, where rst the static nonlinear function is identied, then the FIR coefcients identication step takes place. This approach circumvents the identication of a non-linear system of equations. The block diagram of the wiener model is shown in Figure 4. The Hammerstein model is similar in principle to the Wiener model with interchanging the order of the blocks, where the LTI system precedes the lter; which can be an Innite Impulse Response (IIR) lter [56]. The block Diagram of the Hammerstein model is shown in Figure 5. The input output relation is given by

$$x_{out} = \sum_{j=0}^{M} h(j) G\left(|x_{in}(n-j)|\right) x_{in}(n-j) \tag{5.4}$$

In this model also, the identication steps are similar in order to that of the Wiener model. It was shown in 5 that a PA identied by a Hammerstein model achieves a more accurate estimation than a Wiener model. Also, a Hammerstein predistorter achieves better linearization results.

3) Neural Networks: Neural networks are also used to model digital predistortion for power amplifiers. A two-layers forward neural network has the ability to give a relatively good approximation for any mild nonlinear function [57]. Neural networks are adaptive in nature and can approximate the desired predistortion functions [58]. Nonetheless, the training of the neural network is complex and time-consuming and its implementation in hardware is not easy in practical applications [38]. The mathematical expression of a single neuron is given by

$$y = F(wx + b) \tag{5.5}$$

where x and y are the input and output of the neuron,respectively, w the weight value, b the bias value, and F the activation function. The articial neural network is usually composed of several neurons. They are divided into three types depending on their structure: MultiLayer Perceptron (MLP), Radial Basis Function articial Neural Network (RBFNN) and Recurrent articial Neural Network

(RNN). Several neural network based digital predistortion methods are reported in literature such as in [59][58][38][57][60][61] and [62]. Some early simple designs of neural networks were effective in modeling the nonlinear behavior of the power amplifier however they suffered when strong memory effects were present. Therefore various dynamic neural structures have been proposed especially for wideband signals, where memory effects cannot be ignored. The output of a recurrent neural network that utilizes feedforward and feedback signal processing can be modeled as

$$y(n) = f[y(n-1), y(n-2), y(n-p), x(n), x(n-1), x(n-q)] \tag{5.6}$$

where p and q stand for the memory depth of the power amplifier, x and y are input and output of the network [59]. Figure 6b also shows a focused time-delay neural network (FTDNN) that takes into account that the output of the amplifier depends on present and past input values. It also eliminates the feedback time-delay line by processing present and past inputs . However, the two models suffer from computational complexity because they employ one-input one-output complex waveforms [58].

5.2.2 Challenges to DPD

In current and future networks, more small cells will be deployed to use the limited spectrum resource more efciently. The output power of the power amplifier in these cells will be become lower, thus the consumed power for computing digital predistortion parameters will become signicant. Low-powerconsumption digital predistortion solutions are required [63].

Also, Wide-band digital predistortion is much more challenging than its analog counterpart because the signal with its intermodulation distortion products is limited by the sampling rate of the digital system [43]. As presented in Figure 3, the conversion between the digital data domain and the RF signal includes the digital-to-analog converters (DAC) IQ-modulator and mixer for up-conversion to RF, and driver amplifier in the transmit path, and the downconverter and analog-to-digital converter (ADC) in the feedback path. The predistorted signal has typically a bandwidth ve times the signal bandwidth. This increase in bandwidth constitutes a challenge for the analog path that must be able to handle the wider bandwidth of the predistorted signal [42]. The bandwidth of the coming fth generation (5G) systems will be wider than 160 MHz which implies that multigiga samples per second (GSPS) analog-todigital converters (ADCs) are required [64].

5.2.3 Solutions

In order to solve the bandwidth requirements, several methods are found in the literature. The authors in [65] propose a new approach using reduced band-

width feedback with the direct learning architecture. They demonstrate that their method can achieve DPD linearization bandwidth and performance similar to the full-rate system.

A band-limited digital predistortion technique is proposed in [66] where a band-limiting function is inserted into the general Volterra operators to control the signal bandwidth under modeling. Although this method improves the model accuracy and eliminates the system bandwidth constraints of the conventional DPD techniques, however it requires the use of an extra costly and complex bandpass lter design in the RF chain.

In [67], they propose a predistortion system that uses a twobox architecture based on the cascade of a memory polynomial followed by a memoryless predistortion function. Hence, part of the linearization is done ofine in the memoryless predistorter to remove the static nonlinearity of the device under test. This will decrease the feedback bandwidth in the memory polynomial predistortion sub-function.

Arbitrary sampling rate of the feedback signal is suggested in [68] that results in the same coefcients of DPD as the one calculated from with a high sampling rate feedback signal.

A low-complexity 1-bit observation method for estimation of digital predistortion coefcients is proposed in [64]. The authors note that with the existing ADC technology, it is difcult to achieve high sampling speed and high resolution at the same time. Hence, the 1-bit solution eases the requirement on the ADC reduces the power consumption and the cost of the feedback path. They expect that this technique will attract signicant interest since it will help achieving ultra high sampling speed in 5G systems using only simple comparators.

In [69], a frequency selectable oscillator is used to alleviate the requirement of high sampling rate ADC in the data acquisition loop. The oscillator utilizes switchable capacitors with a digital control scheme.

Multi-Band DPD: One other solution for reducing the sampling rate requirement is to use the multi-band digital predistortion structure where only the bands of interests are captured through the digital predistortion function $H_k(.)$ [70]. However, this multi-band digital predistortion structure has two main disadvantages. First, it has high implementation cost and synchronization requirements because each digital predistortion coefcient is computed using its corresponding feedback loop. In addition, it has high complexity since each digital predistortion block must be constructed from the combinations of all the K bands. Moreover, the selection of the nonlinear terms must takes into account that the spectra of the generated signal should fall into its corresponding frequency band. In [70], an improved multi-band digital predistortion structure is suggested by applying a band-limited ltering approach and reducing the number of feedback loops to only one. The suggested method reduces the cost of the system while maintaining the required linearization results. As shown in Figure 9, the K bands of output $y_1(n_1), y_2(n_2), \ldots, y_K(n_K)$ are captured individually at

time $t_{n_1}, t_{n_2}, \ldots, t_{n_K}$. The output of the power amplifier $y_k(n_k)$ can be represented as:

$$y_k(n_k) = \sum_{p=1}^{P} \sum_{i_1=0}^{M} \cdots \sum_{i_p=0}^{M} h_{p,BL}(i_1, \ldots, i_p) \left(\left(\prod_{j=1}^{p} x(n_k - i_j) \right) * w_k(n_k) \right) \tag{5.7}$$

where $h_{p,BL}(i_1, \ldots, i_p)$ is the same pth-order bandlimited Volterra kernel for every band k, $w_k(.)(i_1, \ldots, i_p)(k = 1, 2, \ldots, K)$ is the band-limiting function centered at carrier frequency f_k. Similarly, an evenly-space multi-band digital predistortion band with one feedback loop is derived in [71]. Furthermore, concurrent dual-band transmitters linearization technique is investigated in [72] where feedback loops using subsampling analog-to-digital converters are used. A new technique is proposed where aliasing between the carriers is allowed to occur.

The authors in [73] implement a digitally assisted subsampler chip for training adaptive predistortion transmitter, specically the subsampler that serves as the downconversion path in adaptive predistorters for 800MHz - 5.8GHz RF power amplifiers. Digital averaging is employed to overcome the noise folding problems of subsampling and to attenuate low-frequency spurious tones. Moreover, they use quadrature sampling to eliminate IQ gain mismatch errors in the feedback path.

Wang et al. take it a step further in [74] and propose a very compact single-chain multi-band digital predistortion model using one under-sampling ADC and a low band-pass lter to replace the conventional digital predistortion feedback paths. The proposed architecture is presented in Figure 10. The ADC employed in the feedback path is undersampled and captures the output analog signal with aliasing. The authors introduce multi-rate time alignment scheme to align the power amplifier and the undersampled output signals in order to estimate the DPD coefcients.

These are some of the various works in the context of Digital Predistortion. In this thesis we do not add a new DPD method to the literature. We adapt the existing MP model to implement it along with our proposed PVA in order to study the performance of the combined system in the next chapter.

5.3 Simulating DPD in our CA-OFDM Transmitter

In this section we demonstrate the application of DPD to our CA-OFDM transmitter. We adapted the MP model for the compromise it provides between memoryless non-linearity and the full Volterra nonlinearity. Also as demonstrated in [55], the MP model provides a similar performance to the VS model with less

complexity. We simulated an LTE release-8 signal, with 20MHz bandwidth using 16 QAM modulation with no cyclic prex (CP) insertion and a Square Root Raised Cosine with a roll-off factor of 0.22 for pulse shaping.

The LTE signal is fed to a power amplifier whose coefcients are listed in 5.8 are obtained from an actual class AB PA. The coefcients of the simulated PA, and the estimated model are up to the 5th order non-linearity and memory depth of 2. We take the first 1000 samples to estimate the DPD coefficients. Thus out of the presented solutions to the DPD problem, we adapt the downsampling techniuque for its simplicity.

$$\begin{array}{ll} h_{10} = 1.0513 + 0.0904j & h_{30} = -0.0542 - 0.2900j \\ h_{50} = -0.9657 - 0.7028j & h_{11} = -0.0680 - 0.0023j \\ h_{21} = 0.2234 + 0.2317j & h_{31} = -0.2451 - 0.3735j \\ h_{12} = 0.0289 - 0.0054j & h_{32} = -0.0621 - 0.0932j \\ h_{52} = 0.1229 + 0.1508j & \end{array} \tag{5.8}$$

After acquiring the signal at the output of the PA, the DPD parameter estimation is achieved through applying the Indirect Learning Approach (ILA) proposed in [75]. ILA is based on the concept of nding a postinverse of the nonlinear model without any predistorter, and then the post distorter is used as a predistorter while removing the postdistorter, as shown in Figure **??**. Recall that the memory polynomial power amplifier can be described by :

$$y(n) = \sum_{k=1}^{K} \sum_{q=0}^{Q} h_{kq} z_{n-q} \left| z_{n-q} \right|^{k-1} \tag{5.9}$$

Where y is the output signal of the PA, z is the output signal of the predistorter and h_kq are the coefcients of the PA model. The polynomials used for building the post and pre-distorters are identical, and since they are linear in the unknown coefcients, the linear least squares (LLS) method can be used for their estimation. First, the output $y(n)$ undergoes gain normalization giving :

$$u_{kq}(n) = \frac{y(n-q)}{G} \left| \frac{(y(n-q))}{G} \right|^{k-1} \tag{5.10}$$

Where G is taken to be the linear gain. Other options for G can be found in [**chani2015new5**]. On the other hand, the output of the predistorter can be written as [50]:

$$\begin{aligned} z &= Ua \\ z &= [z(0), \ldots, z(N-1)] \\ U &= [u_{10}, \ldots, u_{K0}, \ldots, u_{1Q} \ldots, u_{KQ}] \\ u_{kq} &= [u_{kq}(0), \ldots, u_{kq}(N-1)]^T \\ a &= [a_{10}, \ldots, u_{K0}, \ldots, u_{1Q}, \ldots, u_{KQ}]^T \end{aligned} \tag{5.11}$$

Expressing $z(n)$ as a summation yields

$$z(n) = \sum_{k=1}^{K} \sum_{q=0}^{Q} a_{kq} u(n) \tag{5.12}$$

Finally, the LLS solution is given by

$$a = \left(U^H U\right)^{-1} U^H z \tag{5.13}$$

Where $(.)^H$ denotes a complex conjugate transpose.

5.3.1 Power Spectral Density

We compare the Power Spectral Densities (PSDs) of the signals at the input of the power amplifier, at the output of the power amplifier without applying DPD and the signal at the output of the cascade of the DPD-PA. It can be shown from 5.3 that applying DPD shows a satisfactory performance in supressing the spectral regrowth due to the PA non-linearities. In terms of ACPR performance and at a 3dB input power backoff, applying DPD reduced the ACPR from -34.7986dB to -48.0794dB.

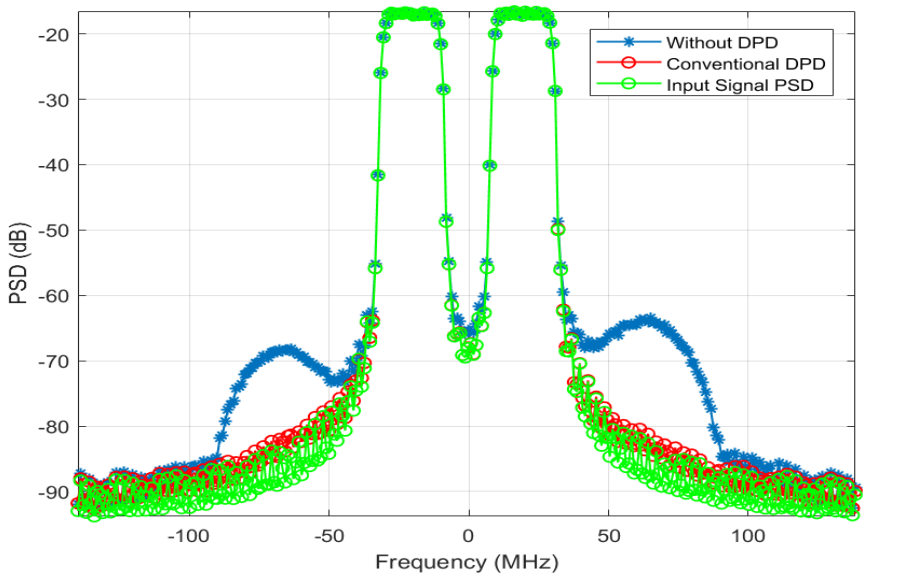

Figure 5.3: Power Spectral Densities at the Input and Output of the PA with and without DPD with CC=2

5.3.2 Adjacent Channel Power Ratio and Input Backoff

We study in this section the ACPR performance as a function of the increase in the average input power. Figure 5.4 shows this relation for the system with and without DPD. First, it can be seen that using DPD remarkably reduces the ACPR value. Second, the ACPR increases with the increase of the average input power, for both systems with and without DPD. However, DPD allows to achieve a constant low ACPR value over a large range of input power. For example, to achieve an ACPR value of -49dB, the system without DPD needs to transmit at an average input power of -23.11dB whereas DPD allows to increase the average input power to -15dB while achieving this ACPR level.

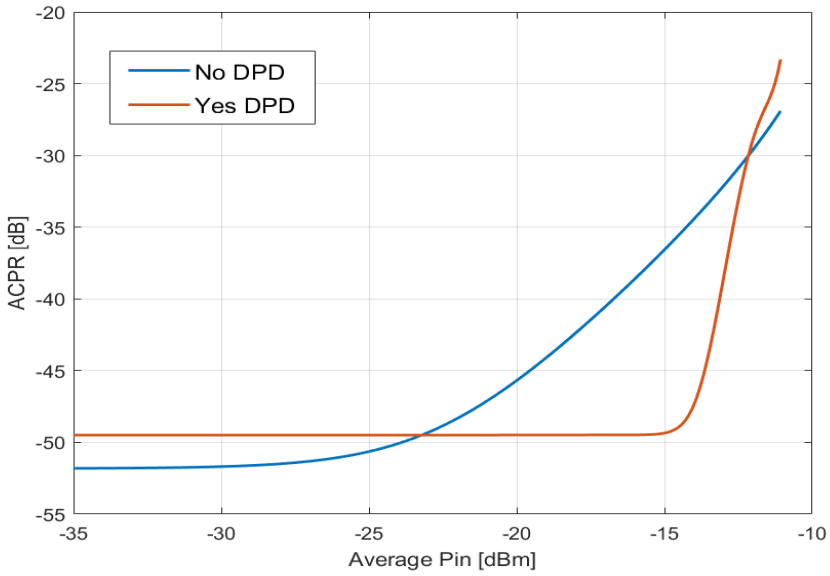

Figure 5.4: ACPR as a function of the IBO

5.4 Chapter Conclusion

This chapter has presented a discussion on Digital Predistortion (DPD) and its challenges, and provided solutions for its mitigation. We thus stated the different works that tackle the two step process of behavioral modeling and inversion of the non-linear effects (linearization), and the solutions to mitigate the DPD challenges. Out of the several existing models for modeling and suppressing the non-linear effects, the Memory Polynomial (MP) model achieves a good trade-off between complexity and performance for both modeling and predistortion. This chapter applied an MP model to linearize the signal to be transmitted. Indirect learning approach (ILA) with Linear Least Square (LLS) was used inorder to

estimate the coefficients of the predistorter. Performance of DPD was studied in terms of spectral regrowth supression and Adjacent Channel Power Ratio (ACPR) reduction. In the next chapter we proceed to analyze the joint combination of PAPR reduction and DPD in order to achieve a trade-off between efficiency and linearity.

Chapter 6

Combining PAPR Reduction and Digital Predistortion

6.1 Chapter Introduction

The aim of this chapter is to study the effect of PAPR reduction on the overall performance of the system. After studying the PAPR distribution and proposing a PAPR reduction technique, we extend the analysis in this chapter to apply the proposed Peak Valley Alignment along side to digital predistortion.

More specifically, we study the effect of PAPR reduction on linearity in terms of Adjacent Channel Power Ratio (ACPR), and on power efficiency in terms of the reduction in the Input Power Back-off (IBO).

We start this chapter by a brief literature review on the works that studied the joint combination of PAPR reduction and Digital Predistortion, then we demonstrate our work in this context.

6.2 A Brief Survey on Joint PAPR Reduction and DPD

Several works have proved either by simulation or theoretically that combining PAPR reduction with Digital Predistortion allows to achieve a better trade-off between efficiency and linearity, thus enhancing the overall performance of the system. [76] provided a theoretical analysis of the trade-off between efficiency and linearity of the PA by deriving the Error Vector Magnitude (EVM) considering PAPR reduction and linearization. Their results indicated that a high performing PAPR reduction technique can slightly enhance the EVM metric. Also, they stated that the maximum possible efficiency is achieved by setting the IBO equal to the PAPR of the signal after PAPR reduction. In [77] the performance of TR-SOCP discussed in chapter 4 was studied in the presence of the PA in terms of

ACPR and BER. Also, it was shown that TR-SOCP enhanced the ACPR. Finally, a recent study in [78] took into consideration in their study the computational complexity. They proposed a new combined PAPR reduction and DPD technique, where they reduce the computational complexity of the system by sacrificing some linearity. Also, they studied the impact of the position of the PAPR reduction block with respect to the DPD block. It was shown that applying PAPR reduction before DPD achieves a better performance than applying it after DPD.

6.3 Peak Valley Alignment and ACPR

It was shown in the previous chapter that using DPD remarkably reduces the ACPR value and that it increases with the increase of the average input power, for both systems with and without DPD. In this section, we demonstrate that the introduction of PAPR reduction indeed enhances the ACPR of the system. Figure 6.1 shows that the combination of PVA and DPD allows to operate near to saturation with a lower ACPR than that achieved with DPD only. Table 6.1

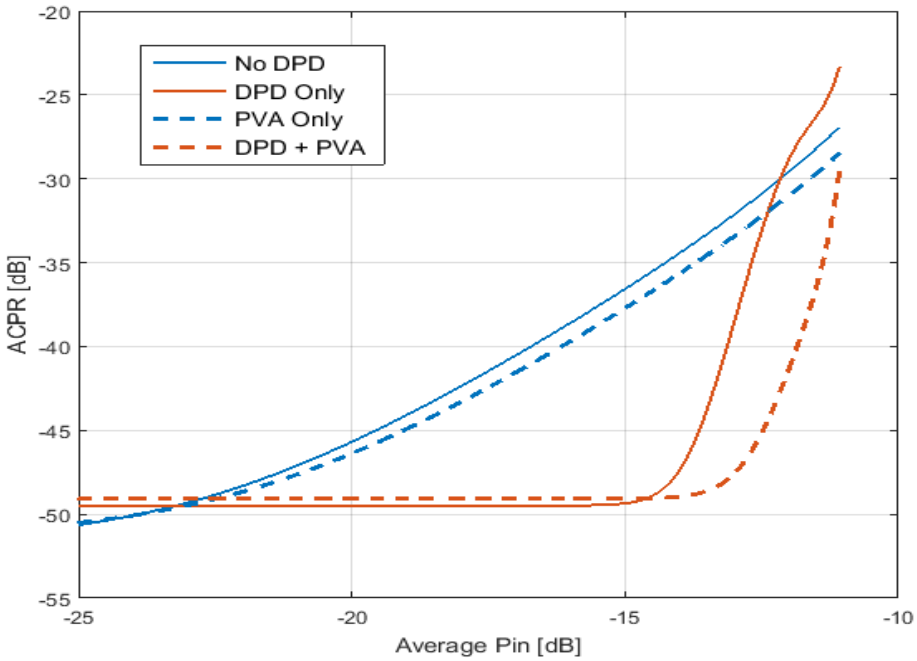

Figure 6.1: ACPR as a function of the Average Input Power

shows that when applying an IBO equals to the amount of the original PAPR of the signal allows the PA to operate in its linear region, but at the cost of a large reduction in the input power. Fortunately, the application of PVA allows to reduce the IBO from 11dB into 7dB, with obtaining approximately the same

Table 6.1: ACPR as a function of IBO at PAPR

Input Power Back-Off [dB]	ACPR without DPD [dB]	ACPR with DPD[dB]
0	-26.9	-23.3
12	-49.5	-49.48
7	-42.4	-49.47
2	-32.14	-38.6

ACPR performance. Note that operating at 0dB IBO refers to operation at saturation. It can be seen that even with DPD, the distortions cannot be mitigated. Finally, the 2dB IBO value refers to an average operation point.

6.4 Peak Valley Alignment and MER

The PAPR performance of the methods are studied by plotting the CCDF functions of PAPR along with the improvement of area of coverage due to PAPR reduction. [35] indicated that relying only on the CCDF for evaluating the performance of a certain PAPR reduction technique is not sufficient. This is because CCDF, which gives the distribution of the PAPR before the HPA, fails to take into account what happens to the signal after it passes through the HPA. Thus for a practical assessment of the system, a more important and convenient metric should be considered. This metric is referred to as the MER (Modulation Error Ratio) or the EVM (Error Vector Magnitude), which are by some means are interchangeable. A signal sent by an ideal transmitter or received by a receiver would have all constellation points precisely at the ideal locations, however various imperfections in the implementation such as the distortion caused by the HPA, cause the actual constellation points to deviate from the ideal locations. The MER therefore is a comparison of the actual location of a received symbol to its ideal location. It is defined as [35]:

$$\mathrm{MER}\{\mathbf{X}, \widehat{\mathbf{X}}\} = 10 \log_{10} \left(\frac{\|\mathbf{X}\|_2^2}{\|\mathbf{X} - \widehat{\mathbf{X}}\|_2^2} \right) \tag{6.1}$$

where $\mathbf{X}$ is the ideal symbol vector measured at the input of the amplifier and is measured at the output of the HPA. The MER results are in agreement with the ACPR results provided in the previous section. Using DPD enhances the MER, and combining DPD with the proposed PVA also slightly enhances the MER.

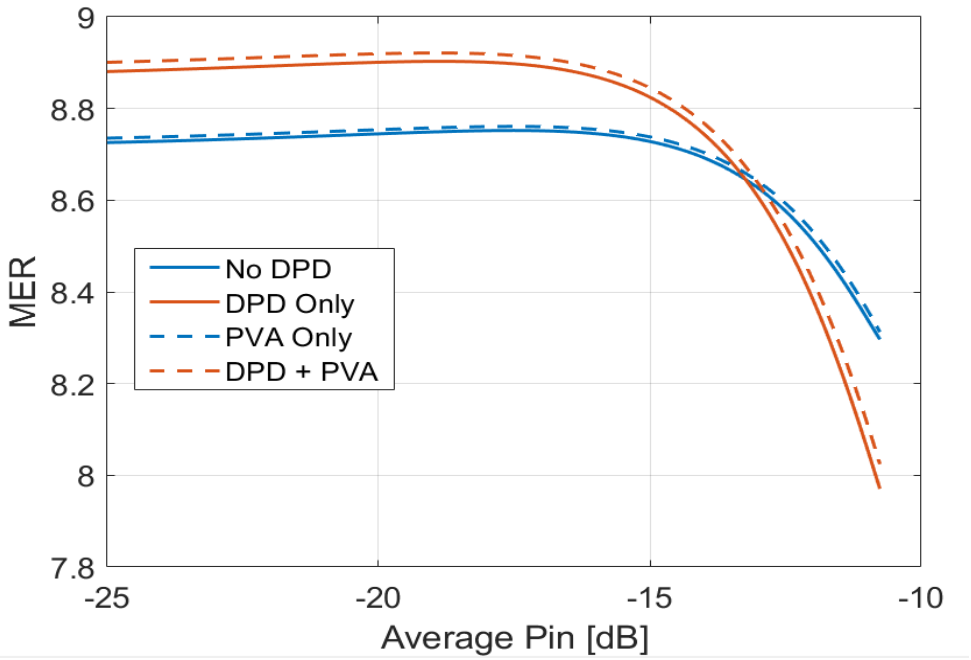

Figure 6.2: MER as a function of the Average Input Power

6.5 Chapter Conclusion

In this chapter, we have combined the proposed Peak Valley Alignment with Digital Predistortion. The ACPR was studied as a function of the average input power. It was shown that combining PVA with DPD allows to operate closer to saturation with a low ACPR. Also, it was demonstrated that PVA allows to achieve a better trade-off between power efficiency and linearity by allowing to operate at a lower IBO.

Chapter 7

Conclusion

The evolving of aggregation of multiple OFDM and SC-FDMA signals will still suffer from high Peak-to-Average-Power-Ratio (PAPR), which in turn will adversely affect and complicate the High Power Amplifier (HPA) design, by inducing out of band emissions, in band distortions and causing decreasing the power efficiency.

This thesis presented a Carrier Aggregated OFDM system that combines PAPR reduction with Digital Predistortion to achieve a good trade-off between efficiency and linearity.

We followed a three step process throughout this thesis. We first analyzed the PAPR of the CA-OFDM system in 3, by deriving an approximation of the probability distribution of PAPR in CA-OFDM systems using level crossing rate analysis, and then we applied the derived expression to model the performance of the Selective Mapping Technique (SLM). We then proposed a new PAPR reduction method in 4, referred to as Peak Valley Alignment. Although we did not apply the LCR approximation to model PVA, we incorporated some of the results to systematize PVA. Through Monte-Carlo simulations, we have shown that PVA achieved a superior PAPR reduction gain to other frequency and time based processing techniques, and a close performance to optimization based techniques. The PAPR reduction gain enhanced the coverage area gain in addition to increasing the power efficiency by reducing the required IBO. We then derived the computational complexity of PVA and showed that it provided a large reduction in computation especially when the number of aggregated component carriers increased.

The second step was conducting a study in 5 to existing linearization techniques and applying the well known technique Digital Predistortion to our system, where the PSDs of the signals at the input and output of the PA with and without DPD were plotted, and spectral regrowth was suppressed by the application of DPD. Then the ACPR was plotted as a function of the average input power. It was demonstrated that DPD allows to operate at a low ACPR with a larger input power, thus closer to saturation.

Finally, we combined the proposed PAPR reduction method with DPD to study the overall system performance, and the combined system had a better performance in terms of ACPR and IBO, where the performance of the system in terms of lowering the Adjacent Channel Power Ratio and lowering the needed Input Backoff thus increasing the power efficiency was enhanced.

For the future work of this thesis, a deeper study shall is to be done regarding the combined system of PAPR reduction and DPD. Also, we shall consider the other performance metric known as the Error Vector Magnitude (EVM), where it allows to study the inband distortion of the system.

Appendix A

Abbreviations

OFDM	Orthogonal Frequency division Multiplexing
LTE	Long Term Evolution
CA	Carrier Aggregation
SC-FDMA	Single Carrier Frequency Division Multiplexing
HetNets	Hetergenuous Networks
TDD	Time Division Duplex
FDD	Frequency Division Duplex
eCA	enhanced Carrier Aggregation
PAPR	Peak-To-Average-Power-Ratio
HPA	High Power Amplifier
RF	Radio Frequency
IFFT	Inverse Fast Fourier Transform
LTE-A	Long Term Evolution Advanced
CC	Component Carrier
CP	Cyclic Prefix
i.i.d	Independent Identically Distributed
IMD	Intermodulation Distortion
DPD	Digital Predistortion
LCR	Level Crossing Rate
CDF	Cumulative Density function
NC-OFDM	Non Contiguous Orthogonal Frequency division Multiplexing
PSD	Power Spectral Density
CF	Crest Factor
QAM	Quadrature Amplitude Modulation
RB	Resource Blocks
SLM	Selective Mapping Technique
PVA	Peak Valley Alignment
D/A	Digital to analog
PSLM	Partial Selective Mapping
KLT	KarhunenLove Theorem

TR-SOCP	Tone Reservation Second Order Cone Programming
PRS	Peak Reducing Signals
CSP	Circular Shifts Partition
FFT	Fast Fourier Transform
DFT	Discrete Fourier Transform
MB-OFDM	Multi Band Orthogonal Frequency division Multiplexing
CCDF	Complementary Cumulative Density function
AWGN	Additive White Gaussian Noise
BER	Bit Error Rate
SNR	Signal to Noise Ratio
eNodeB	Evolved Node B
RMUL	Real Multiplication
RADD	Real Addition
IPM	Interior Point Methods
TWTA	Traveling-Wave Tube Amplifier
SSPA	Solid State Power Amplifier
OOB	Out of Band Emissions
ACPR	Adjacent Channel Power Ratio
NMSE	Normalized Mean Square Error
LUT	Look Up Table
VS	Volterra Series
PCA	Principle Component Analysis
CS	Compressive Sensing
MP	Memory Polynomia
GMP	Generalized Memory Polynomial
DDR	Dynamic Deviation Reduction
FIR	Finite Impulse Response
LTI	Linear Time Invariant
IIR	Infinite Impulse Response
MLP	Multi Layer Perceptron
RBFANN	Radial Basis Function Artificial Neural Network
RNN	Recurrent Artificial Neural Network
FTDNN	Focused Time-Delay Neural Network
DAC	Digital to Analog Converter
IQ	Inphase Quadrature
ADC	Analog to Digital Converter
5G	Fifth Generation
ILA	Indirect Learning Approach
LLS	Linear LEast Squares
IBO	Input Power Backoff
EVM	Error Vector Magnitude

References

[1] H. Ochiai and H. Imai, "On the distribution of the peak-to-average power ratio in ofdm signals," *IEEE transactions on communications*, vol. 49, no. 2, pp. 282–289, 2001.

[2] M. Issa, A.-k. Ajami, H. Artail, and Y. Nasser, "An approximation for the distribution of the peak-to-average power ratio in carrier-aggregated ofdm signals using level crossing rate analysis," in *Wireless and Mobile Computing, Networking and Communications (WiMob),*, IEEE, 2017, pp. 1–8.

[3] C. Tellambura, "Upper bound on peak factor of n-multiple carriers," *Electronics letters*, vol. 33, no. 19, pp. 1608–1608, 1997.

[4] S. Shepherd, J. Orriss, and S. Barton, "Asymptotic limits in peak envelope power reduction by redundant coding in orthogonal frequency-division multiplex modulation," *IEEE Transactions on Communications*, vol. 46, no. 1, pp. 5–10, 1998.

[5] R. Van Nee and A. De Wild, "Reducing the peak-to-average power ratio of ofdm," in *Vehicular technology conference, 1998. VTC 98. 48th IEEE*, IEEE, vol. 3, 1998, pp. 2072–2076.

[6] S. Wei, D. L. Goeckel, and P. E. Kelly, "A modern extreme value theory approach to calculating the distribution of the peak-to-average power ratio in ofdm systems," in *Communications, 2002. ICC 2002. IEEE International Conference on*, IEEE, vol. 3, 2002, pp. 1686–1690.

[7] R. Rajbanshi, A. M. Wyglinski, and G. J. Minden, "Peak-to-average power ratio analysis for nc-ofdm transmissions," in *Vehicular Technology Conference, 2007. VTC-2007 Fall. 2007 IEEE 66th*, IEEE, 2007, pp. 1351–1355.

[8] A. Kliks and P. Kryszkiewicz, "On the crest factor approximation of noncontiguous ofdm signal," in *Wireless Communication Systems (ISWCS), 2015 International Symposium on*, IEEE, 2015, pp. 71–75.

[9] P. Kryszkiewicz, A. Kliks, and Y. Louet, "Papr analysis in noncontiguous ofdm systems," *Transactions on Emerging Telecommunications Technologies*, vol. 28, no. 6, e3133, 2017.

[10] D. Wulich and L. Goldfeld, "Bound of the distribution of instantaneous power in single carrier modulation," *IEEE transactions on wireless communications*, vol. 4, no. 4, pp. 1773–1778, 2005.

[11] H. G. Myung, *Single carrier orthogonal multiple access technique for broadband wireless communications*, 2007.

[12] S. Daumont, B. Rihawi, and Y. Lout, "Root-raised cosine filter influences on papr distribution of single carrier signals," in *Communications, Control and Signal Processing, 2008. ISCCSP 2008. 3rd International Symposium on*, IEEE, 2008, pp. 841–845.

[13] M. Tanahashi and H. Ochiai, "On the distribution of instantaneous power in single-carrier signals," *IEEE Transactions on Wireless Communications*, vol. 9, no. 3, 2010.

[14] H. Ochiai, "On instantaneous power distributions of single-carrier fdma signals.," *IEEE Wireless Commun. Letters*, vol. 1, no. 2, pp. 73–76, 2012.

[15] ——, "Statistical distributions of instantaneous power and peak-to-average power ratio for single-carrier fdma systems," *Physical communication*, vol. 8, pp. 47–55, 2013.

[16] P. Yen, H. Minn, and C.-C. Chong, "Papr reduction for bandwidth-aggregated ofdm and sc-fdma systems," in *Wireless Communications and Networking Conference (WCNC), 2011 IEEE*, IEEE, 2011, pp. 1363–1368.

[17] S. O. Rice, "Mathematical analysis of random noise," *Bell System Technical Journal*, vol. 24, no. 1, pp. 46–156, 1945.

[18] S. H. Crandall, "Zero crossings, peaks, and other statistical measures of random responses," *The Journal of the Acoustical Society of America*, vol. 35, no. 11, pp. 1693–1699, 1963.

[19] S. Wei, D. L. Goeckel, and P. A. Kelly, "Convergence of the complex envelope of bandlimited ofdm signals," *IEEE Transactions on Information Theory*, vol. 56, no. 10, pp. 4893–4904, 2010.

[20] C. Tellambura, "Computation of the continuous-time par of an ofdm signal with bpsk subcarriers," *IEEE Communications letters*, vol. 5, no. 5, pp. 185–187, 2001.

[21] R. W. Bauml, R. F. Fischer, and J. B. Huber, "Reducing the peak-to-average power ratio of multicarrier modulation by selected mapping," *Electronics letters*, vol. 32, no. 22, pp. 2056–2057, 1996.

[22] T. Jiang, D. Qu, and P. Gao, "Distribution of peak-to-average power ratio and its applications in ofdm systems with unequal power allocation," in *Wireless Internet Conference (WICON), 2010 The 5th Annual ICST*, IEEE, 2010, pp. 1–9.

[23] Y. Rahmatallah and S. Mohan, "Peak-to-average power ratio reduction in ofdm systems: A survey and taxonomy," *IEEE communications surveys & tutorials*, vol. 15, no. 4, pp. 1567–1592, 2013.

[24] B. Fehri, S. Boumaiza, and E. Sich, "Crest factor reduction of inter-band multi-standard carrier aggregated signals," *IEEE Transactions on Microwave Theory and Techniques*, vol. 62, no. 12, pp. 3286–3297, 2014.

[25] P. Yen and H. Minn, "Low complexity papr reduction methods for carrier-aggregated mimo ofdma and sc-fdma systems," *EURASIP Journal on Wireless Communications and Networking*, vol. 2012, no. 1, p. 179, 2012.

[26] A.-k. Ajami, H. A. Artail, and M. M. Mansour, "A low-complexity papr reduction technique for lte-advanced uplink with carrier aggregation," in *Global Communications Conference (GLOBECOM), 2015 IEEE*, IEEE, 2015, pp. 1–6.

[27] A.-k. Ajami and H. A. Artail, "A stochastic optimization technique for papr reduction in the uplink of lte-advanced with carrier aggregation," in *Information and Communication Systems (ICICS), 2017 8th International Conference on*, IEEE, 2017, pp. 204–209.

[28] L. Kewen and X. Ning, "Papr reduction of uplink for carrier aggregation in lte-advanced," in *Information Science and Engineering (ICISE), 2010 2nd International Conference on*, IEEE, 2010, pp. 2224–2226.

[29] A.-k. Ajami and H. A. Artail, "Klt-based papr reduction technique for lte-advanced uplink with carrier aggregation," in *Wireless and Mobile Computing, Networking and Communications (WiMob), 2015 IEEE 11th International Conference on*, IEEE, 2015, pp. 514–519.

[30] S. Hussain, "Peak to average power ratio analysis and reduction of cognitive radio signals," PhD thesis, Université Rennes 1, 2009.

[31] P. O. Börjesson, H. G. Feichtinger, N. Grip, M. Isaksson, N. Kaiblinger, P. Odling, and L.-E. Persson, "Dmt par-reduction by weighted cancellation waveforms," *Proc. Radiovetenskaplig Konferens*, pp. 303–307, 1999.

[32] R. Durbin, S. R. Eddy, A. Krogh, and G. Mitchison, *Biological sequence analysis: Probabilistic models of proteins and nucleic acids*. Cambridge university press, 1998.

[33] S. Uliel, A. Fliess, and R. Unger, "Naturally occurring circular permutations in proteins," *Protein engineering*, vol. 14, no. 8, pp. 533–542, 2001.

[34] J. G. Proakis and D. K. Manolakis, *Digital signal processing (4th edition)*. Upper Saddle River, NJ, USA: Prentice-Hall, Inc., 2006, ISBN: 0131873741.

[35] S. K. C. Bulusu, M. Crussière, J.-F. Hélard, R. Mounzer, Y. Nasser, O. Rousset, and A. Untersee, "Quasi-optimal tone reservation papr reduction algorithm for next generation broadcasting systems: A performance/complexity/latency tradeoff with testbed implementation," *IEEE Transactions on Broadcasting*, 2018.

[36] B. Gordillo, F. Sandoval, P. Ludeña-González, and K. Rohoden, "Increase the range and coverage on ofdm system using papr reduction by clipping on sdr," in *2018 IEEE Third Ecuador Technical Chapters Meeting (ETCM)*, IEEE, 2018, pp. 1–6.

[37] F. Li, "Linearization of power amplifiers in wide band communication systems by digital baseband predistortion technique," PhD thesis, UNIVERSITE DE NANTES, 2012.

[38] X. Feng, "Efficient baseband digital predistortion techniques for linearizing power amplifier by taking into account nonlinear memory effect," PhD thesis, université de Nantes, 2015.

[39] A. Katz, "Linearization: Reducing distortion in power amplifiers," *IEEE microwave magazine*, vol. 2, no. 4, pp. 37–49, 2001.

[40] F. Zavosh, M. Thomas, C. Thron, T. Hall, D. Artusi, D. Anderson, D. Ngo, and D. Runton, "Digital predistortion techniques for rf power amplifiers with cdma applications," *Microwave Journal*, vol. 42, no. 10, p. 12, 1999.

[41] A. Grebennikov, *Rf and microwave transmitter design*. John Wiley & Sons, 2011, vol. 234.

[42] J. Wood, "Digital pre-distortion of rf power amplifiers: Progress to date and future challenges," in *Microwave Symposium (IMS), 2015 IEEE MTT-S International*, IEEE, 2015, pp. 1–3.

[43] A. Grebennikov, N. O. Sokal, and M. J. Franco, *Switchmode rf and microwave power amplifiers*. Academic Press, 2012.

[44] J. K. Cavers, "Amplifier linearization using a digital predistorter with fast adaptation and low memory requirements," *IEEE transactions on vehicular technology*, vol. 39, no. 4, pp. 374–382, 1990.

[45] K. J. Muhonen, M. Kavehrad, and R. Krishnamoorthy, "Look-up table techniques for adaptive digital predistortion: A development and comparison," *IEEE transactions on vehicular technology*, vol. 49, no. 5, pp. 1995–2002, 2000.

[46] R. Braithwaite, "Digital predistortion of an rf power amplifier using a reduced volterra series model with a memory polynomial estimator," *IEEE Transactions on Microwave Theory and Techniques*, vol. 65, no. 10, pp. 3613–3623, 2017.

[47] A. Zhu and T. J. Brazil, "Behavioral modeling of rf power amplifiers based on pruned volterra series," *IEEE Microwave and Wireless components letters*, vol. 14, no. 12, pp. 563–565, 2004.

[48] A. Abdelhafiz, A. Kwan, O. Hammi, and F. M. Ghannouchi, "Digital predistortion of lte-a power amplifiers using compressed-sampling-based unstructured pruning of volterra series," *IEEE Transactions on Microwave Theory and Techniques*, vol. 62, no. 11, pp. 2583–2593, 2014.

[49] P. L. Gilabert, G. Montoro, D. Lopez, N. Bartzoudis, E. Bertran, M. Payaro, and A. Hourtane, "Order reduction of wideband digital predistorters using principal component analysis," in *Microwave Symposium Digest (IMS), 2013 IEEE MTT-S International*, IEEE, 2013, pp. 1–7.

[50] L. Ding, G. T. Zhou, D. R. Morgan, Z. Ma, J. S. Kenney, J. Kim, and C. R. Giardina, "A robust digital baseband predistorter constructed using memory polynomials," *IEEE Transactions on communications*, vol. 52, no. 1, pp. 159–165, 2004.

[51] M. Schetzen, "Nonlinear system modeling based on the wiener theory," *Proceedings of the IEEE*, vol. 69, no. 12, pp. 1557–1573, 1981.

[52] J. Kim and K. Konstantinou, "Digital predistortion of wideband signals based on power amplifier model with memory," *Electronics Letters*, vol. 37, no. 23, pp. 1417–1418, 2001.

[53] D. R. Morgan, Z. Ma, J. Kim, M. G. Zierdt, and J. Pastalan, "A generalized memory polynomial model for digital predistortion of rf power amplifiers," *IEEE Transactions on signal processing*, vol. 54, no. 10, pp. 3852–3860, 2006.

[54] A. Zhu, J. C. Pedro, and T. J. Brazil, "Dynamic deviation reduction-based volterra behavioral modeling of rf power amplifiers," *IEEE Transactions on microwave theory and techniques*, vol. 54, no. 12, pp. 4323–4332, 2006.

[55] F. M. Ghannouchi and O. Hammi, "Behavioral modeling and predistortion," *IEEE Microwave Magazine*, vol. 10, no. 7, pp. 52–64, 2009.

[56] P. L. Gilabert Pinal, G. Montoro López, and E. Bertran Albertí, "On the wiener and hammerstein models for power amplifier predistortion," in *Asia-Pacific Microwave Conference (APMC'05)*, Institute of Electrical and Electronics Engineers (IEEE), 2005.

[57] Y. Qian and F. Liu, "Neural network predistortion technique for nonlinear power amplifiers with memory," in *Communications and Networking in China, 2006. ChinaCom'06. First International Conference on*, IEEE, 2006, pp. 1–5.

[58] M. Rawat, K. Rawat, and F. M. Ghannouchi, "Adaptive digital predistortion of wireless power amplifiers/transmitters using dynamic real-valued focused time-delay line neural networks," *IEEE Transactions on Microwave Theory and Techniques*, vol. 58, no. 1, pp. 95–104, 2010.

[59] D. Luongvinh and Y. Kwon, "Behavioral modeling of power amplifiers using fully recurrent neural networks," in *Microwave Symposium Digest, 2005 IEEE MTT-S International*, IEEE, 2005, 4–pp.

[60] Z. Huang, W. Chen, Z. Feng, and F. M. Ghannouchi, "Forward behavioral modeling of concurrent dual-band power amplifiers using extended real valued time delay neural networks," in *Microwave and Millimeter Wave Technology (ICMMT), 2012 International Conference on*, IEEE, vol. 5, 2012, pp. 1–4.

[61] B. O'Brien, J. Dooley, and T. J. Brazil, "Rf power amplifier behavioral modeling using a globally recurrent neural network," in *2006 IEEE MTT-S International Microwave Symposium Digest*, IEEE, 2006, pp. 1089–1092.

[62] S. Boumaiza and F. Mkadem, "Wideband rf power amplifier predistortion using real-valued time-delay neural networks," in *Microwave Conference, 2009. EuMC 2009. European*, IEEE, 2009, pp. 1449–1452.

[63] L. Guan and A. Zhu, "Green communications: Digital predistortion for wideband rf power amplifiers," 2014.

[64] H. Wang, G. Li, C. Zhou, W. Tao, F. Liu, and A. Zhu, "1-bit observation for direct-learning-based digital predistortion of rf power amplifiers," *IEEE Transactions on Microwave Theory and Techniques*, vol. 65, no. 7, pp. 2465–2475, 2017.

[65] L. Ding, F. Mujica, and Z. Yang, "Digital predistortion using direct learning with reduced bandwidth feedback," in *Microwave Symposium Digest (IMS), 2013 IEEE MTT-S International*, IEEE, 2013, pp. 1–3.

[66] C. Yu, L. Guan, E. Zhu, and A. Zhu, "Band-limited volterra series-based digital predistortion for wideband rf power amplifiers," *IEEE Transactions on Microwave Theory and Techniques*, vol. 60, no. 12, pp. 4198–4208, 2012.

[67] O. Hammi, A. Kwan, S. Bensmida, K. A. Morris, and F. M. Ghannouchi, "A digital predistortion system with extended correction bandwidth with application to lte-a nonlinear power amplifiers," *IEEE Transactions on Circuits and Systems I: Regular Papers*, vol. 61, no. 12, pp. 3487–3495, 2014.

[68] Z. Wang, S. Ibrahim, H. Su, and R. Farrell, "Generalised digital predistortion of rf power amplifiers with low-rate feedback signal," in *Microwave Conference (EuMC), 2016 46th European*, IEEE, 2016, pp. 831–834.

[69] K. McGrath and A. Zhu, "A 2.0–2.5 ghz frequency-selectable oscillator for digital predistortion model identification of rf power amplifiers," in *Integrated Nonlinear Microwave and Millimetre-wave Circuits Workshop (INMMiC), 2017*, IEEE, 2017, pp. 1–3.

[70] C. Yu and A. Zhu, "Single feedback loop-based digital predistortion for linearizing concurrent multi-band transmitters," in *IEEE MTT-S Int. Microw. Symp. Dig.*, 2014, pp. 1–3.

[71] G. Su and W. Chen, "Digital predistortion for concurrent multi-band pas with inter-band imd compensation," in *Electromagnetics: Applications and Student Innovation Competition (iWEM), 2016 IEEE International Workshop on*, IEEE, 2016, pp. 1–3.

[72] A. Prata, D. C. Ribeiro, P. M. Cruz, A. S. Oliveira, and N. B. Carvalho, "Rf subsampling feedback loop technique for concurrent dual-band pa linearization," *IEEE Transactions on Microwave Theory and Techniques*, vol. 64, no. 12, pp. 4174–4182, 2016.

[73] S. Chung and J. L. Dawson, "A 73.1 db sndr digitally assisted subsampler for rf power amplifier linearization systems," in *VLSI Circuits, 2009 Symposium on*, IEEE, 2009, pp. 148–149.

[74] Z. Wang, L. Guan, and R. Farrell, "Compact undersampled digital predistortion for flexible single-chain multi-band rf transmitter," in *Microwave Symposium (IMS), 2017 IEEE MTT-S International*, IEEE, 2017, pp. 1542–1545.

[75] C. Eun and E. J. Powers, "A new volterra predistorter based on the indirect learning architecture," *IEEE transactions on signal processing*, vol. 45, no. 1, pp. 223–227, 1997.

[76] O. A. Gouba and Y. Louet, "Theoretical analysis of the trade-off between efficiency and linearity of the high power amplifier in ofdm context," in *EW 2012*, 2012, 7–p.

[77] I. M. Mahafeno, Y. Louët, and J.-F. Helard, "Peak-to-average power ratio reduction using second order cone programming based tone reservation for terrestrial digital video broadcasting systems," *IET communications*, vol. 3, no. 7, pp. 1250–1261, 2009.

[78] S. Wang, M. Roger, and C. Lelandais-Perrault, "Impacts of crest factor reduction and digital predistortion on linearity and power efficiency of power amplifiers," *IEEE Transactions on Circuits and Systems II: Express Briefs*, 2018.